

1 **Cloud-radiative impact on the regional responses of the**  
2 **mid-latitude jet streams and storm tracks to global**  
3 **warming**

4 **Nicole Albern<sup>1</sup>, Aiko Voigt<sup>1,2</sup>, Joaquim G. Pinto<sup>1</sup>**

5 <sup>1</sup>Institute of Meteorology and Climate Research - Department Troposphere Research, Karlsruhe Institute  
6 of Technology, Karlsruhe, Germany

7 <sup>2</sup>Lamont-Doherty Earth Observatory, Columbia University, New York, USA

8 **Key Points:**

- 9 • We investigate global atmosphere model simulations in present-day setup with pre-  
10 scribed SST and the cloud-locking method
- 11 • Cloud-radiative impact on jet response is substantial, and largely independent of  
12 season and SST pattern, but depends on the ocean basin
- 13 • Cloud-radiative impact is zonally symmetric, consistent with a zonally symmet-  
14 ric change in cloud-radiative heating in the mid-latitudes

---

Corresponding author: Nicole Albern, [nicole.albern@kit.edu](mailto:nicole.albern@kit.edu)

## 15 **Abstract**

16 Previous work demonstrated the strong radiative coupling between clouds and the mid-  
17 latitude circulation. Here, we investigate the impact of cloud-radiative changes on the  
18 global warming response of the mid-latitude jet streams and storm tracks in the North  
19 Atlantic, North Pacific and Southern Hemisphere. To this end, we use the ICON global  
20 atmosphere model in present-day setup and with the cloud-locking method. Sea surface  
21 temperatures (SST) are prescribed to isolate the circulation response to atmospheric cloud-  
22 radiative heating. In the annual mean, cloud-radiative changes contribute one- to two-  
23 thirds to the poleward jet shift in all three ocean basins, and support the jet strength-  
24 ening in the North Atlantic and Southern Hemisphere. Cloud-radiative changes also im-  
25 pact the storm track, but the impact is more diverse across the three ocean basins. The  
26 cloud-radiative impact on the North Atlantic and North Pacific jets varies little from sea-  
27 son to season in absolute terms, whereas its relative importance changes over the course  
28 of the year. In the Southern Hemisphere, cloud-radiative changes strengthen the jet in  
29 all seasons, whereas their impact on the jet shift is limited to austral summer and fall.  
30 The cloud-radiative impact is largely zonally-symmetric and independent of whether global  
31 warming is mimicked by a uniform 4 K or spatially-varying SST increase. Our results  
32 emphasize the importance of cloud-radiative changes for the response of the mid-latitude  
33 circulation to global warming, indicating that clouds can contribute to uncertainty in  
34 model projections of future circulations.

## 35 **1 Introduction**

36 The mid-latitude jet streams and storm tracks dominate the heat, momentum and  
37 moisture transport outside of the tropics (Hoskins & Valdes, 1990; Chang et al., 2002;  
38 Shaw et al., 2016). They are important components of the large-scale atmospheric cir-  
39 culation, because of which understanding their responses to global warming is essential  
40 for reliable predictions of regional climate change (e.g., Ulbrich et al., 2009). Jet streams  
41 and storm tracks, and their responses to global warming, were studied extensively dur-  
42 ing the last decades (e.g., Kushner et al., 2001; Yin, 2005; Chang et al., 2012; Barnes &  
43 Polvani, 2013; Simpson et al., 2014). Nevertheless, climate model projections of future  
44 changes in jets and storm tracks exhibit large uncertainties (Shepherd, 2014), and the  
45 factors controlling the location, strength and variability of jet streams and storm tracks  
46 remain not fully understood (Bony et al., 2015; Vallis et al., 2015; Shaw et al., 2016).

47 Here, we focus on the coupling of clouds with the mid-latitude circulation, and study the  
48 role of cloud-radiative changes for the global warming response of the jet streams and  
49 storm tracks.

50 Global climate models suggest that the jet streams and storm tracks shift poleward  
51 in both hemispheres and that the Southern Hemisphere jet streams and storm tracks strengthen  
52 in response to global warming (e.g., Yin, 2005; Pinto et al., 2006; Chang et al., 2012; Barnes  
53 & Polvani, 2013; Simpson et al., 2014; Vallis et al., 2015). The response of the mid-latitude  
54 circulation is related to changes in meridional temperature gradients and baroclinicity.  
55 As such, previous work studied the role of increased upper-tropospheric and decreased  
56 lower-tropospheric temperature gradients (e.g., Yin, 2005; Lorenz & DeWeaver, 2007;  
57 Butler et al., 2010; Harvey et al., 2015). These temperature changes can result from a  
58 multitude of factors, including moist convection (Vallis et al., 2015), ozone depletion (Polvani  
59 et al., 2011), and sea-ice loss (Vavrus, 2018; Zappa et al., 2018).

60 An additional factor that strongly projects on meridional temperature gradients  
61 are clouds and their radiative interactions. Cloud-radiative interactions were found to  
62 set the latitude of the Southern Hemisphere jet stream (Ceppi et al., 2012) and strengthen  
63 the jet streams in present-day climate (Li et al., 2015). The poleward shifts of the South-  
64 ern Hemisphere storm track and eddy-driven jet stream in global warming simulations  
65 were found to depend on the radiative response of Southern Ocean clouds (Ceppi et al.,  
66 2014; Grise & Polvani, 2014b; Ceppi & Shepherd, 2017). Li et al. (2019) found that at-  
67 mospheric cloud-radiative effects enhance the poleward jet shift in response to global warm-  
68 ing in present-day simulations that apply the COOKIE framework (Clouds On-Off Kli-  
69 mate Intercomparison Experiment; Stevens et al., 2012). Idealized global warming sim-  
70 ulations in aquaplanet setups revealed that half or more of the poleward jet stream shift  
71 can be attributed to cloud-radiative changes (Voigt & Shaw, 2015; Ceppi & Hartmann,  
72 2016). The aquaplanet work of Voigt & Shaw (2015) and Voigt & Shaw (2016) identi-  
73 fied that cloud-radiative changes are important even when sea surface temperatures (SST)  
74 are prescribed, showing that a large part of the cloud-radiative impact results from the  
75 direct atmospheric cloud-radiative heating. This is supported by the study of Voigt et  
76 al. (2019), which investigated the cloud-radiative impact on the annual-mean zonal-mean  
77 jet stream response in a present-day setup. The authors decomposed the cloud-radiative  
78 impact into a surface and an atmospheric pathway, depending on whether SST are in-  
79 teractive or prescribed. They found that the atmospheric pathway of the cloud-radiative

80 impact, i.e. the impact of changes in atmospheric cloud-radiative heating in the absence  
81 of SST changes, is at least as important as the surface pathway, i.e. the response of the  
82 surface temperature to surface cloud-radiative heating.

83 Given the importance of continents for shaping the mid-latitude circulation (Brayshaw  
84 et al., 2009), we extend the aquaplanet studies and investigate the impact of cloud-radiative  
85 changes on the global warming response of the mid-latitude jet streams and storm tracks  
86 in more realistic simulations that include present-day boundary conditions, i.e., conti-  
87 nents, sea ice, and a seasonal cycle. These simulations further allow us to study the cloud-  
88 radiative impact across seasons and ocean basins. This is important as the mid-latitude  
89 circulation response varies substantially over the course of the year and across regions  
90 (Simpson et al., 2014; Zappa et al., 2015).

91 We investigate the impact of cloud-radiative changes on the annual-mean and seasonal-  
92 mean responses of the mid-latitude jet streams and storm tracks to global warming in  
93 the North Atlantic, North Pacific and Southern Hemisphere ocean. For this purpose, we  
94 perform simulations with the ICOSahedral Nonhydrostatic model (ICON; Zängl et al.,  
95 2015) and estimate the role of cloud-radiative changes with the cloud-locking method  
96 (e.g., Voigt & Shaw, 2015; Ceppi & Hartmann, 2016; Voigt & Shaw, 2016). SST are pre-  
97 scribed to isolate the impact of cloud-radiative changes when clouds do not affect SST,  
98 complementing the work of Ceppi & Shepherd (2017) with interactive SST. We compare  
99 two sets of global warming simulations that use different SST changes to mimic global  
100 warming. This allows us to study to what extent the cloud-radiative impact depends on  
101 the pattern of the surface warming, which Woollings et al. (2012) identified to shape the  
102 storm track response in the North Atlantic and over Europe.

103 We address the following questions:

- 104 • How important is the cloud-radiative impact for the mid-latitude jet stream and  
105 storm track responses to global warming in the North Atlantic, North Pacific, and  
106 Southern Hemisphere ocean?
- 107 • To what extent does the cloud-radiative impact vary across seasons and ocean basins?
- 108 • Does the cloud-radiative impact depend on the pattern of the SST increase?

109 The structure of the paper is as follows: Section 2 presents the model setup, the  
110 metrics for the mid-latitude jet streams and storm tracks, and the application of the cloud-

locking method to diagnose the impact of cloud-radiative changes. The annual-mean responses are discussed in Section 3; the seasonal-mean responses are covered in Section 4. In Section 5 we show correlations between the jet stream and atmospheric temperature gradients. The main results are summarized and discussed in Section 6.

## 2 Model Setup, Circulation Metrics and Cloud-Locking Method

### 2.1 Model Setup and Mid-latitude Circulation Metrics

We perform numerical simulations with the atmospheric component of ICON (Zängl et al., 2015). The model is run with the physics package used for numerical weather prediction (version 2.1.00). The simulations are performed in R2B04 horizontal resolution (approximately 160 km) with 47 levels extending up to 75 km. A time step of 720 s is used.

We use a present-day model setup with prescribed SST. SST are prescribed to isolate atmospheric cloud-radiative interactions, which primarily arise from longwave radiation (Allan, 2011). We use climatological SST and sea ice fields, which are obtained by calculating multi-year monthly-means of the SST and sea ice fields over the AMIP period (1979-2008; Gates, 1992). The multi-year monthly-means are prescribed to the model in the control simulation (“CTL”). The annual-mean SST pattern of the control simulation is shown in Fig. 1 (left panel). In addition, we perform two sets of global warming simulations. In the first set, global warming is mimicked by a uniform 4 K SST increase (“UNI”), similar to the Amip4K simulations that are part of the Coupled Model Intercomparison Project Phase 5 (CMIP5; Taylor et al., 2012). In the second set, global warming is mimicked by increasing the SST by a pattern (“PAT”), similar to the Amip-Future simulations in CMIP5. We use the same SST pattern that is used for the Amip-Future simulations, and which is provided by CFMIP (Cloud Feedback Model Intercomparison Project) at <https://www.earthsystemcog.org/projects/cfmip/cfmip2-cmip5>. The SST pattern is derived from the multi-model mean SST response simulated by CMIP3 global atmosphere-ocean models at the time of CO<sub>2</sub> quadrupling in the 1% CO<sub>2</sub> increase per year experiment (Taylor et al., 2009, 2012). The SST pattern is scaled to a global mean of 4 K so that both UNI and PAT experience the same global-mean SST increase. In contrast to UNI, however, PAT includes changes in the SST gradients as represented in the CMIP3 multi-model mean. Thus, the SST impact derived from the PAT simulations implicitly includes the surface pathway of the cloud-radiative heating. Fig. 1 (right

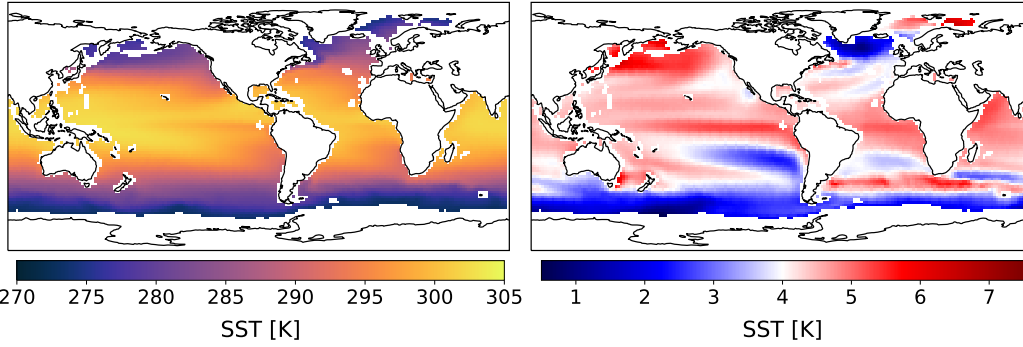


**Figure 1.** Annual-mean SST pattern of the CTL simulation (left) and anomalous SST pattern used for the PAT simulation (right). Regions covered by land or more than 15% of sea ice are masked.

142 panel) shows the anomalous annual-mean SST pattern used in PAT. Compared to the  
 143 uniform 4 K SST increase, the SST increase in PAT is about 1-2 K larger in the Trop-  
 144 ics, the northern North Pacific and the Barents Sea. At the same time, SST is hardly  
 145 increased south of Greenland (subpolar gyre), in the Southern Ocean and in the east-  
 146 ern South Pacific.

147 To isolate the effect of increased SST, sea ice is set to control values in all simu-  
 148 lations and atmospheric greenhouse gas concentrations are kept constant ( $\text{CO}_2 = 390$  ppmv,  
 149  $\text{CH}_4 = 1800$  ppbv,  $\text{N}_2\text{O} = 322$  ppbv,  $\text{CFC}_{11} = 240$  pptv,  $\text{CFC}_{12} = 532$  pptv). We use  
 150 the GEMS (Global and Regional Earth-System Monitoring using Satellite and In-Situ  
 151 Data; Hollingsworth et al., 2008) ozone climatology from the European Centre for Medium-  
 152 Range Weather Forecast (ECMWF) Integrated Forecast System (IFS) model. Aerosols  
 153 are specified according to Tegen et al. (1997). For every simulation, we run the model  
 154 for 31 years, with the first year being excluded from the analysis to avoid model initial-  
 155 ization effects.

156 We quantify the mid-latitude circulation and its response to global warming based  
 157 on the mid-latitude jet streams and storm tracks. Following Barnes & Polvani (2013)  
 158 we define the latitude and strength of the mid-latitude jet streams based on the max-  
 159 imum zonal wind at 850 hPa,  $u_{850}$ . In the Northern (Southern) Hemisphere, we search  
 160 for the maximum  $u_{850}$  between  $25^\circ\text{N}$  and  $70^\circ\text{N}$  ( $25^\circ\text{S}$  and  $70^\circ\text{S}$ ), and perform a quadratic  
 161 fit around the maximum and its two neighboring grid points on an interpolated  $0.01^\circ$

162 latitude grid. The maximum of the quadratic fit yields the jet strength,  $u_{jet}$ , and its po-  
163 sition the jet latitude,  $\varphi_{jet}$ . For ocean-basin mean values of the jet and its response to  
164 global warming, the calculation of the jet latitude and jet strength is based on the zonal-  
165 mean  $u_{850}$  field over the longitudinal boundaries of the respective ocean basin (see be-  
166 low for definition of boundaries). For maps of the  $u_{850}$  response shown in Section 3,  $\varphi_{jet}$   
167 is calculated at each longitude. To make the comparison between the two hemispheres  
168 easier, all latitudes for the Northern Hemisphere are shown in “degrees North”, and all  
169 latitudes for the Southern Hemisphere in “degrees South”. Thus, for both hemispheres,  
170 a positive change in  $\varphi_{jet}$  indicates a poleward jet shift.

171 We further characterize the storm tracks, which measure the synoptic activity of  
172 the mid-latitude atmosphere (e.g., Hoskins & Valdes, 1990; Christoph et al., 1995; Chang  
173 et al., 2002; Yin, 2005; Pinto et al., 2007; Ulbrich et al., 2008; Shaw et al., 2016). While  
174 their magnitude and variability are dominated by transient low pressure systems, they  
175 also contain some variability associated with high pressure systems (which typically have  
176 longer time scales). We calculate the storm tracks from the standard deviation of the  
177 2.5 to 6 day bandpass filtered 500 hPa geopotential height field (e.g., Blackmon, 1976),  
178 using the bandpass filter of the Climate Data Operators (CDO, version 1.9.4., available  
179 at <https://www.mpimet.mpg.de/cdo>).

180 We focus our analysis on the three major ocean basins of the Earth. These are the  
181 North Atlantic (60°W-0°), the North Pacific (135°E-125°W), and the Southern Hemi-  
182 sphere Ocean (all longitudes). The longitudinal boundaries of the ocean basins are the  
183 same as in Barnes & Polvani (2013).

184 The left column of Fig. 2 shows the global-warming response of the annual-mean  
185 zonal-mean circulation in UNI. The model simulates the changes expected from global  
186 coupled atmosphere-ocean models (e.g., Lu et al., 2008; Ma & Xie, 2013; Grise & Polvani,  
187 2014a; Harvey et al., 2015). This includes amplified upper-tropospheric warming in the  
188 tropics (Fig. 2a) and a vertical expansion of the troposphere, which manifests in upward  
189 shifts of the upper-level jet streams (Fig. 2c) and the upper boundary of the Hadley cells  
190 (Fig. 2e). ICON also simulates a weakening and horizontal expansion of the tropics, which  
191 are indicated by a poleward shift of the mid-latitude jet streams in the lower and mid-  
192 dle troposphere (Fig. 2c) and a weakening and poleward expansion of the Hadley cells  
193 (Fig. 2e). Very similar results are also found in the PAT simulation (Fig. S1). Note, how-

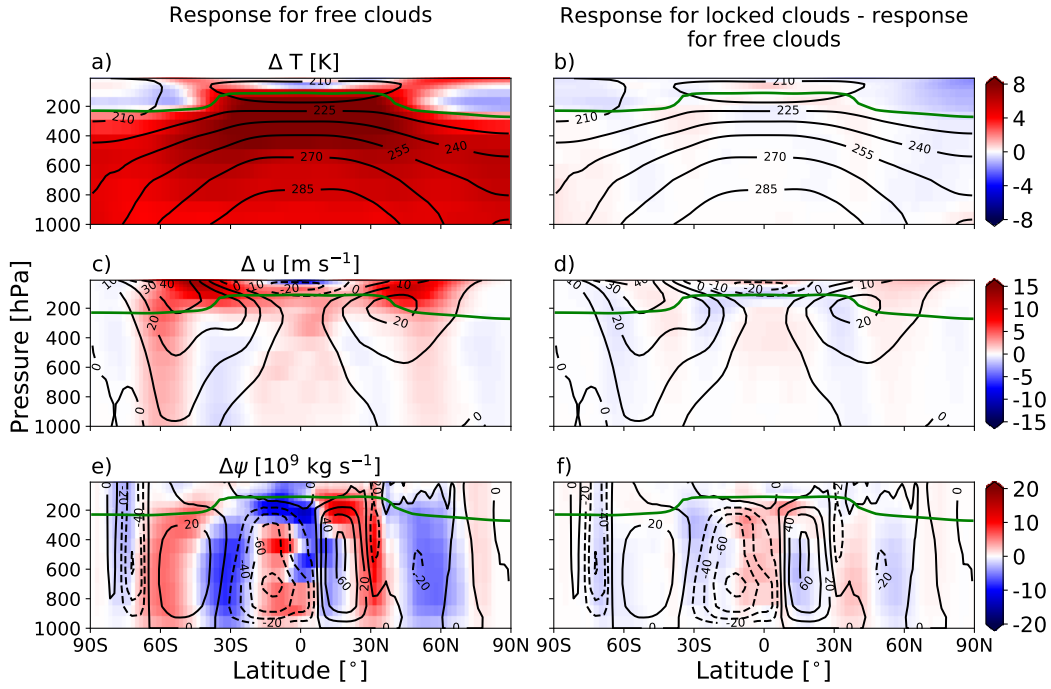


**Figure 2.** Response of the annual-mean zonal-mean atmospheric temperature (top), zonal wind (middle), and mass stream function (bottom) to a uniform SST increase with free clouds (left) (UNI-CTL). The right column shows the difference between the response in the locked and free simulations. The green line in each panel shows the tropopause height in the control simulation CTL.

194 ever, that the Southern Hemisphere Hadley cell strengthens in the PAT simulation. The  
 195 zonal-mean zonal wind response in our model is consistent with the annual-mean zonal-  
 196 mean zonal wind response in atmosphere global climate models with fixed SST, in which  
 197 global warming is mimicked by the spatially varying SST increase of the CMIP5 Amip-  
 198 Future setup (e.g., compare Fig. 2c and Fig. S1c to Fig. 5 right in Grise & Polvani, 2014a).

## 199 2.2 Cloud-locking method

200 We use the cloud-locking method to quantify the impact of cloud-radiative changes  
 201 on the response of the mid-latitude circulation to global warming. The method allows  
 202 us to break the radiative interactions and feedbacks between clouds and the circulation  
 203 by prescribing the radiative properties of clouds to the model's radiative transfer scheme  
 204 (e.g., Voigt & Shaw, 2015). While originally devised to study the impact of radiative feed-

205 backs on global-mean and regional surface warming (e.g., Wetherald & Manabe, 1988;  
206 Schneider et al., 1999; Langen et al., 2012; Mauritsen et al., 2013), the locking method  
207 has become a helpful tool to investigate the contribution of cloud-radiative changes to  
208 circulation changes (Voigt & Shaw, 2015; Ceppi & Hartmann, 2016; Voigt & Shaw, 2016;  
209 Voigt et al., 2019).

210 In a first step, we diagnose the instantaneous cloud-radiative properties (i.e., cloud  
211 water, cloud ice and cloud fraction) in the CTL, UNI and PAT simulations. Because cloud-  
212 radiative effects are non-linear functions of cloud-radiative properties, we store the lat-  
213 ter at every call of the radiative transfer scheme (every 36 minutes), as was done in pre-  
214 vious studies (e.g., Voigt & Shaw, 2015; Ceppi & Hartmann, 2016). We store ten years  
215 of cloud data to adequately sample cloud variability.

216 In a next step, we simulate 30 years with cloud-radiative properties prescribed to  
217 values from CTL, UNI or PAT. We cycle three times through the 10 years of stored cloud  
218 fields. We have checked that this does not introduce any spurious periodicity to the mid-  
219 latitude circulation in the prescribed-clouds simulations. The “cloud locking” only af-  
220 fects the radiative transfer scheme. All other components of ICON use the internally sim-  
221 ulated clouds. The prescribed cloud-radiative properties are offset by at least one year  
222 relative to the simulated climate of the model to achieve a spatiotemporal decorrelation  
223 of the cloud-radiative properties and the atmospheric circulation, temperature and mois-  
224 ture. This decorrelation might result in situations in which a cloud free subsidence re-  
225 gion is simulated by the model, but the radiation scheme is run with cloud-radiative prop-  
226 erties of a deep convective cloud at the same time. The impact of this decorrelation on  
227 the climatological circulation is found to be mainly small in our simulations. This is in  
228 line with other studies that used the cloud-locking method to investigate the circulation  
229 response to global warming (Voigt & Shaw, 2015, 2016; Ceppi & Hartmann, 2016; Ceppi  
230 & Shepherd, 2017; Voigt et al., 2019).

231 To quantify the cloud-radiative contribution to the circulation change in the UNI  
232 simulation, we perform the four additional simulations T1C1, T1C2, T2C1, and T2C2.  
233 The numbers indicate whether SST (T) and cloud-radiative properties (C) are prescribed  
234 to values from CTL (simulation 1) or UNI (simulation 2). With this, we decompose the  
235 circulation response into a contribution from the SST increase, assuming no changes in  
236 the cloud-radiative properties, and a contribution from changes in the cloud-radiative

237 properties assuming no SST increase. The total response of any given variable  $X$  to the  
 238 combined effect of a uniform SST increase and cloud-radiative changes is given by

$$\Delta X = X_{UNI} - X_{CTL} = X_{T2C2} - X_{T1C1} + Res, \quad (1)$$

239 where  $X_{UNI}$  and  $X_{CTL}$  denote the simulations with free clouds, and  $Res$  is the resid-  
 240 ual due to the application of the cloud-locking method (see below for more explanations).

241 The contribution of the SST increase is given by

$$\Delta X_{SST} = \frac{1}{2} [(X_{T2C1} - X_{T1C1}) + (X_{T2C2} - X_{T1C2})], \quad (2)$$

242 and is referred to as ‘‘SST impact’’ hereafter. Analogously, the contribution of cloud-radiative  
 243 changes, hereafter referred to as ‘‘cloud-radiative impact’’, is given by

$$\Delta X_{clouds} = \frac{1}{2} [(X_{T1C2} - X_{T1C1}) + (X_{T2C2} - X_{T2C1})]. \quad (3)$$

244 By construction, the SST and cloud-radiative impact sum up to  $X_{T2C2} - X_{T1C1}$ , so that  
 245  $\Delta X = \Delta X_{SST} + \Delta X_{clouds} + Res$ . The cloud-radiative impact in the PAT simulation  
 246 is quantified in an analogous manner.

247 Importantly, the residual  $Res$  in general is found to be much smaller than  $\Delta X$ . This  
 248 can be verified by comparing CTL and UNI with ‘‘free’’ clouds to their ‘‘locked’’ coun-  
 249 terparts T1C1 and T2C2, for which the prescribed cloud-radiative properties are decor-  
 250 related from the circulation (Fig. 2, right). The fact that the residual  $Res$  of the lock-  
 251 ing method is small, implies that the locking method can be used to meaningfully sep-  
 252 arate SST and cloud-radiative impacts.

253 While the zonal-mean circulation and jet stream responses to global warming in  
 254 the North Pacific and Southern Hemisphere are similar in the simulations with free and  
 255 locked clouds, larger differences occur for the jet response over the North Atlantic in the  
 256 annual-mean, and during boreal winter (December to February, DJF) and spring (March  
 257 to May, MAM) (Fig. S2). During these seasons, the North Atlantic jet stream of the con-  
 258 trol simulation is located more equatorward for locked clouds than for free clouds. This  
 259 is possibly related to decreased convective activity over the Maritime Continent and west-  
 260 ern tropical Pacific when clouds are locked, as indicated by increased outgoing longwave  
 261 radiation and decreased high level cloud cover (not shown; e.g., Cassou, 2008; Hender-  
 262 son et al., 2016). At the same time, the North Atlantic jet stream of the UNI and PAT  
 263 simulations is located more poleward when clouds are locked. This is possibly related

264 to enhanced warming of North America in the simulations with locked clouds (not shown;  
265 Ceppi et al., 2018). As a result, in these seasons the North Atlantic jet shift in the locked  
266 simulations is larger than in the free simulations, and larger than what is commonly sim-  
267 ulated by coupled climate models. However, we are mainly interested in quantifying the  
268 impact of cloud-radiative changes in relation to the total (locked) response. Also, the  
269 magnitude of the cloud-radiative impact appears to be less sensitive to the jet position  
270 in the control simulation. This can be seen by comparing the cloud-radiative impact for  
271 each ocean basin across seasons (see Section 4). Although the seasons differ with respect  
272 to the control jet position (Fig. S2), the cloud-radiative impact is similar across seasons,  
273 especially in the Northern Hemisphere (see Section 4 for a more detailed discussion of  
274 the results).

275 The residual between the jet responses in the simulations with free and locked clouds  
276 can either be caused by internal variability or by the decorrelation due to the applica-  
277 tion of the cloud-locking method. To check that the difference between the simulations  
278 is a result of the large internal variability, and to verify that the ocean basin mean jet  
279 stream responses with free and locked clouds are statistically similar, we analyze their  
280 difference for the annual-mean and each season. To this end, we calculate the bootstrap  
281 distributions for the difference between the jet responses in the simulations with free and  
282 locked clouds (see Supplementary Text S1 and Fig. S3 for a more detailed description of  
283 the methodology). Fig. 3 shows the mean difference between the jet responses in the free  
284 and locked simulations for both global warming setups in each ocean basin and season.  
285 In the North Pacific and Southern Hemisphere, the jet latitude and jet strength responses  
286 are statistically similar on a 95% significance level and close to zero during most sea-  
287 sons. In the North Atlantic, however, large differences between the jet latitude response  
288 in the free and locked simulations occur in the annual-mean, DJF and MAM. The largest  
289 differences are present in MAM, pointing to a decorrelation effect due to the application  
290 of the cloud-locking method in this season. Thus, the results for the jet latitude response  
291 in MAM should be interpreted with caution.

292 We have shown that the residual between the jet responses in the simulations with  
293 free and locked clouds is small and that the jet response in the simulations with free and  
294 locked clouds are statistically similar during most seasons and ocean basins. In the fol-  
295 lowing Sections, we will show the results for the simulations with locked clouds, so that  
296 the SST impact and cloud-radiative impact sum up to the total response.

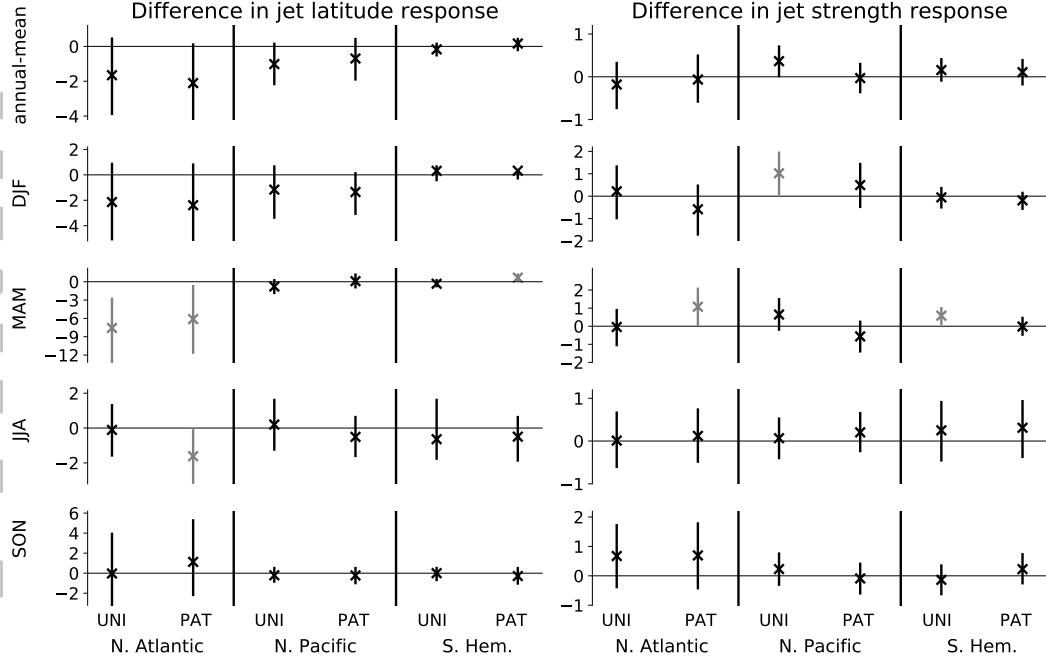


**Figure 3.** Mean (crosses) and 95 % significance level (vertical lines) for the difference in the jet latitude (left) and jet strength (right) responses between simulations with free clouds and simulations with locked clouds. Results are shown for each season, ocean basin and global warming setup. Black symbols indicate that the responses in simulations with locked and free clouds are statistically similar, grey symbols indicate that they are not statistically similar on a 95 % level. Note the different ranges for the vertical axes of the panels.

### 297 2.3 Change in cloud-radiative heating

298 We perform a forward Partial-Radiative Perturbation (PRP) calculation (Wether-  
 299 ald & Manabe, 1988) to diagnose the change in cloud-radiative heating due to cloud-radiative  
 300 changes between the CTL and UNI simulations, and between the CTL and PAT sim-  
 301 ulations. The change in cloud-radiative heating is calculated by contrasting the radia-  
 302 tive heating rates from CTL with those derived by prescribing UNI or PAT clouds to an  
 303 atmosphere with otherwise CTL properties. Thus, the change in cloud-radiative heat-  
 304 ing  $\partial T/\partial t$  is given by

$$\left. \frac{\partial T(\varphi, \vartheta, p)}{\partial t} \right|_{\text{PRP}} = R(T_{\text{CTL}}, q_{\text{CTL}}, c_{\text{UNI/PAT}}) - R(T_{\text{CTL}}, q_{\text{CTL}}, c_{\text{CTL}}), \quad (4)$$

305 where  $R$  is the radiative heating rate, and  $T$ ,  $q$ , and  $c$  are atmospheric temperature, spe-  
 306 cific humidity and cloud-radiative properties at latitude  $\varphi$ , longitude  $\vartheta$  and pressure  $p$ .

307 The subscripts *CTL* and *UNI/PAT* indicate whether the variables are taken from the  
308 control and global-warming simulations, respectively. The change in cloud-radiative heat-  
309 ing is calculated for every grid point at every call of the radiation scheme for a 5 year  
310 period.

### 311 **3 Annual-mean circulation response**

312 In this section, we study the annual-mean response of the mid-latitude circulation  
313 in the UNI and PAT simulations based on the total response in the prescribed-clouds  
314 setup and the decomposition of the response into a cloud-radiative impact and an SST  
315 impact. The zonal wind at 850 hPa and the storm tracks undergo significant changes in  
316 response to both a uniform (Fig. 4a, d) and a patterned SST increase (Fig. 5a, d). For  
317 the zonal wind shown in the left panels, the black lines indicate the control jet latitude.  
318 In the right panels, the grey contours show the storm track in the control simulation.  
319 Statistical significance of the responses is indicated by dots, and is calculated with a two-  
320 sided t-test for two samples and using a p-value of 0.05 (95 % confidence interval).

321 We have verified that the annual-mean total responses in UNI and PAT are in line  
322 with the robust responses in the CMIP5 Amip4K and AmipFuture simulations (Figs. S4-  
323 S5, top rows; Grise & Polvani, 2014a). Differences to the robust annual-mean responses  
324 in the CMIP5 models occur mainly in the eastern North Pacific where ICON shows a  
325 poleward jet shift, whereas the CMIP5 models show a weakening of the jet, and in the  
326 Southern Hemisphere east of South America (in UNI) where ICON shows a jet strength-  
327 ening and the CMIP5 models show a poleward shift. These differences result in a slightly  
328 overestimated annual-mean poleward jet shift in the North Pacific and reduced poleward  
329 jet shift in the Southern Hemisphere in both global warming setups (Figs. S6-S7).

330 Fig. 4a shows the total response in the UNI simulations. In the North Pacific, changes  
331 in  $u_{850}$  indicate a poleward jet shift in the western and eastern parts of the ocean basin  
332 and a strengthening in the central part. In the North Atlantic, the wind response is more  
333 zonal, with a poleward jet shift across the ocean basin and a strengthening in the jet exit  
334 region over Europe. In the Southern Hemisphere, the jet exhibits a poleward shift at most  
335 longitudes, and a strengthening south of Australia and southeast of South America.

336 Decomposing the total response into SST and cloud-radiative impacts reveals that  
337 in all three ocean basins a substantial part of the mid-latitude zonal wind response, and

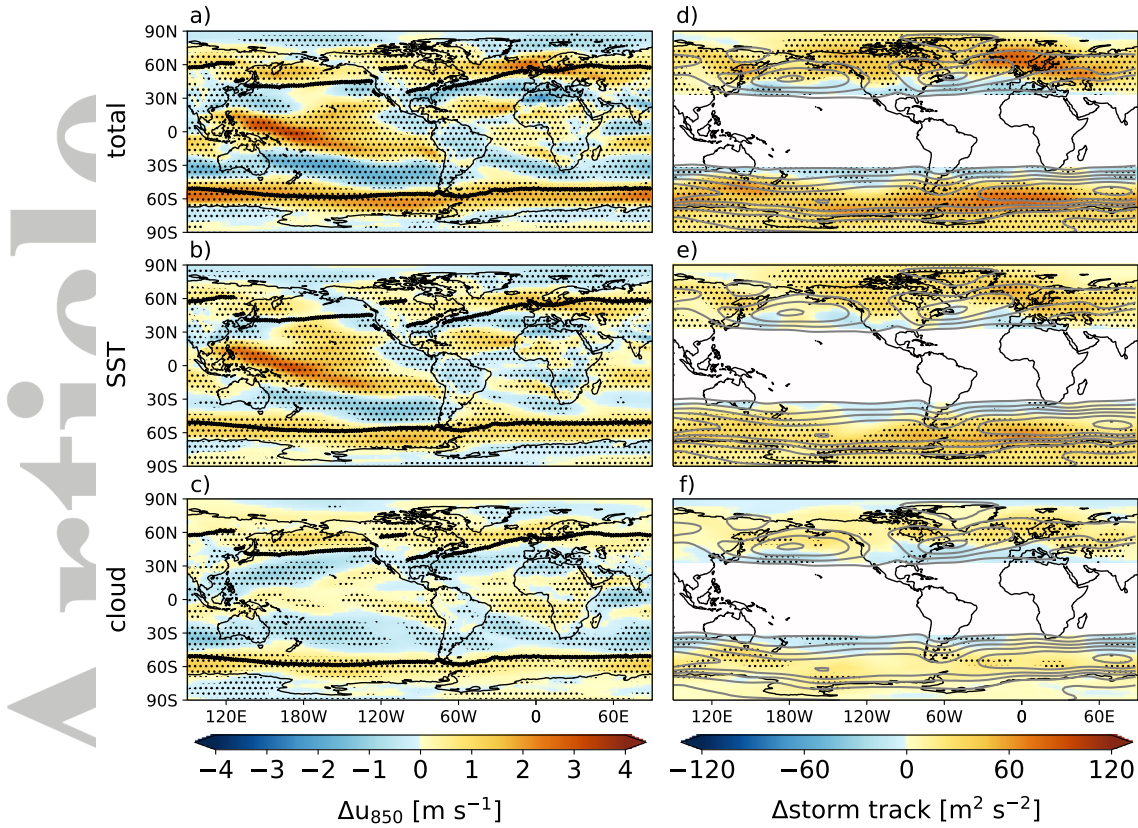


**Figure 4.** Annual-mean response of the 850 hPa zonal wind,  $u_{850}$ , (left) and storm track (right) in the UNI simulations. The total response (top) is decomposed into the SST impact (middle) and the cloud-radiative impact (bottom). The black line in the left column indicates the jet latitude in the control simulation, the grey contours in the right column show the storm track in the control simulation (contour interval of  $100 \text{ m}^2 \text{ s}^{-2}$ ). For the storm track, the Tropics are not shown. The dots indicate where the response is significant at 95 % level.

338 hence jet shift, is attributed to the cloud-radiative impact (Fig. 4c). Remarkably, the cloud-  
 339 radiative impact is almost zonally symmetric in all three ocean basins. In contrast, the  
 340 SST impact is much more zonally asymmetric (Fig. 4b). For example, the jet strength-  
 341 ening over Europe results from the SST impact.

342 The total storm track response is in line with the total  $u_{850}$  response (Fig. 4d). The  
 343 storm track exhibits a poleward shift in the North Pacific, and a poleward shift in the  
 344 North Atlantic with a strengthening in the exit region over Europe. In the Southern Hemi-  
 345 sphere, the storm track strengthens at most longitudes, with decreased storm activity  
 346 on its equatorward flank. This total storm track response is consistent with Ulbrich et

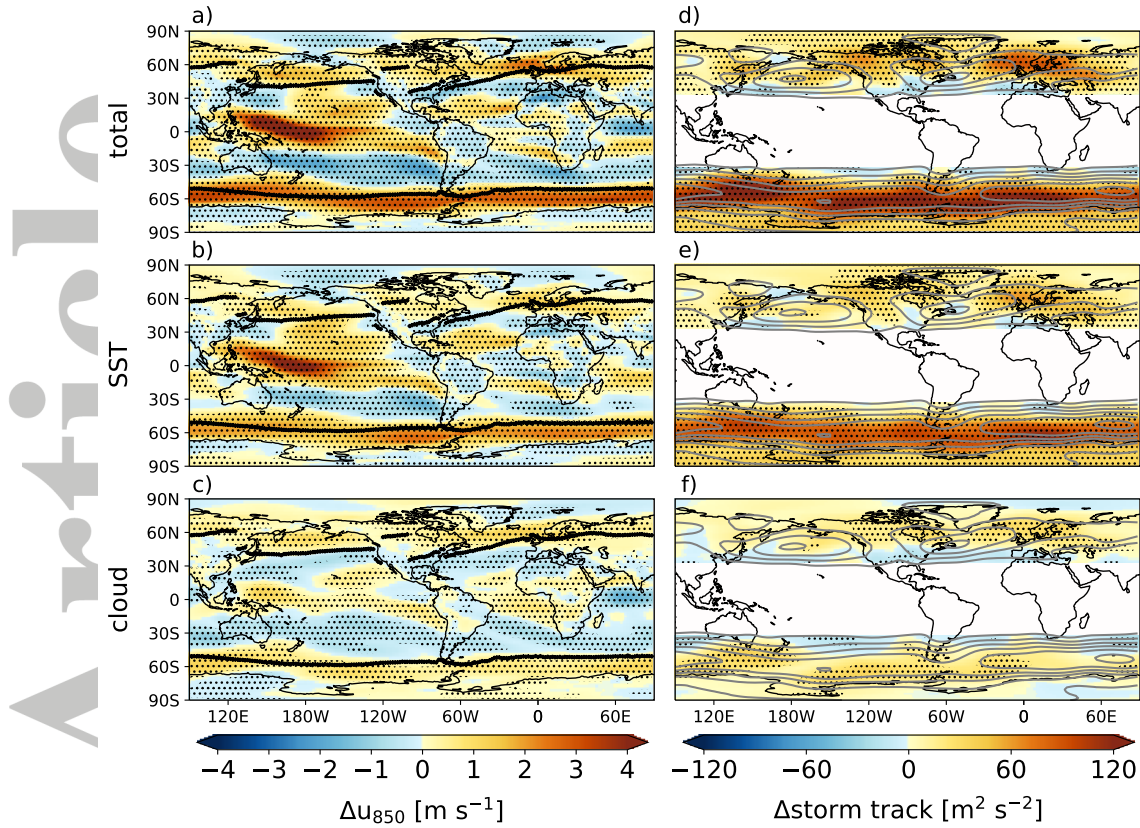


**Figure 5.** Same as Fig. 4, but for the PAT simulations.

347 al. (2009). As for  $u_{850}$ , the cloud-radiative impact is nearly zonally symmetric in all three  
 348 ocean basins (Fig. 4f). The cloud-radiative impact dominates the poleward storm track  
 349 shift in the North Pacific, and is strong in the North Atlantic and over Europe. As for  
 350  $u_{850}$ , the SST impact on the storm track response shows a more complicated spatial struc-  
 351 ture (Fig. 4e).

352 Fig. 5 shows the analogous responses in the PAT simulations. Using a patterned  
 353 instead of a uniform SST increase leads to a somewhat larger total response and SST  
 354 impact in the North Pacific and Southern Hemisphere for both the  $u_{850}$  and storm track  
 355 responses (also see Fig. S8). In the North Atlantic, the total response and SST impact  
 356 are slightly reduced for  $u_{850}$ , and increased in the exit region of the storm track. The  
 357 cloud-radiative impact on the zonal wind and storm track responses, in contrast, is very  
 358 similar between the PAT and UNI simulations in all ocean basins.

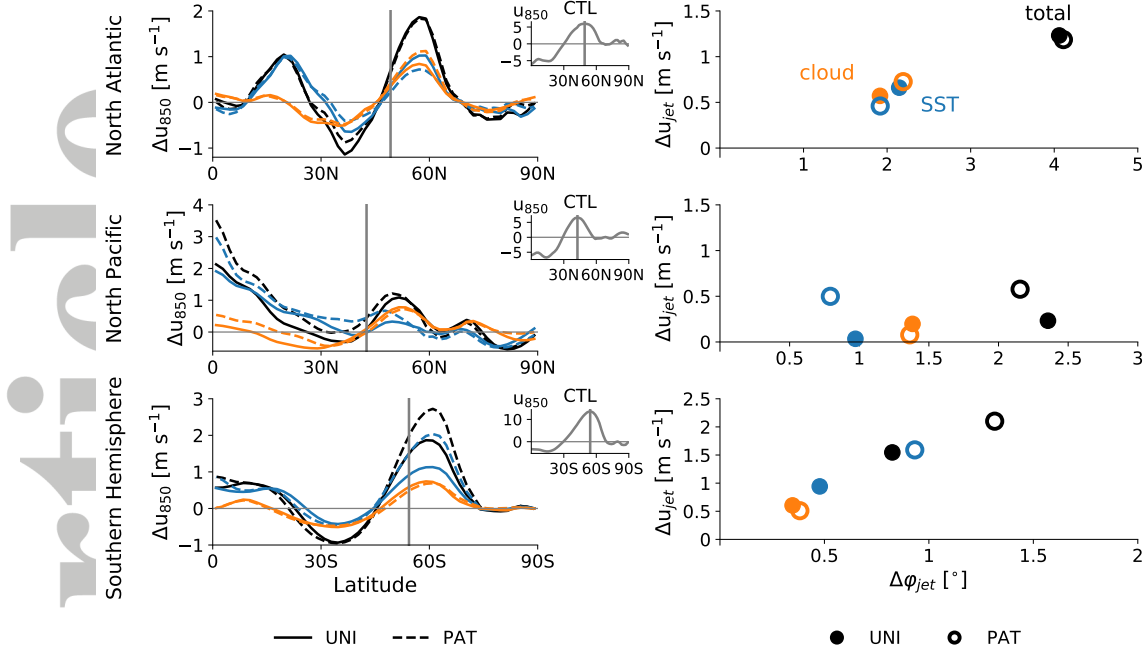


**Figure 6.** The left panels show the annual-mean response of ocean basin zonal-mean  $u_{850}$  in UNI (straight lines) and PAT (dashed lines). The grey bars indicate the jet latitude in CTL derived from the maximum in  $u_{850}$  (small inserted figures). The right panels show the poleward jet shift  $\Delta\phi_{jet}$  versus jet strengthening  $\Delta u_{jet}$ . Results are shown for the North Atlantic (top), North Pacific (middle) and Southern Hemisphere (bottom). The total locked response (black) is decomposed into cloud-radiative impact (orange) and SST impact (blue).

359 To allow for a more quantitative analysis, we quantify the response of the jet latitude  
 360 and jet strength by calculating the zonal-mean  $u_{850}$  response over the three ocean  
 361 basins, using the longitudinal sectors given in Section 2. Fig. 6 shows the ocean-basin zonal-  
 362 mean  $u_{850}$  response, and the associated poleward jet shift and jet strengthening.  $u_{850}$   
 363 of CTL is shown in small insets for reference. The  $u_{850}$  response shows a dipole pattern  
 364 around the control jet latitude (grey bars in Fig. 6, left), with a less pronounced dipole  
 365 in the North Pacific than in the other two ocean basins. The dipole pattern is found for  
 366 the total response, the SST impact, and the cloud-radiative impact, and is consistent with  
 367 a poleward jet shift in all three ocean basins and a jet strengthening in the North At-  
 368 lantic and Southern Hemisphere (Fig. 6, right). In the North Atlantic and Southern Hemi-  
 369 sphere, an almost linear relationship between the poleward jet shift and the jet strength-  
 370 ening is found.

371 The cloud-radiative impact on the jet response, measured in absolute values, is very  
372 similar in UNI and PAT. This shows that in all three ocean basins the cloud-radiative  
373 impact is largely independent of the spatial pattern of SST increase. At the same time,  
374 the relative importance of the cloud-radiative impact is modulated by the pattern of SST  
375 increase in the Southern Hemisphere. In the Southern Hemisphere, the cloud-radiative  
376 impact contributes more than one-third to the jet response in UNI, but less than one-  
377 third in PAT. This results from a stronger total response and stronger SST impact in  
378 PAT compared to UNI, consistent with increased SST gradients (see Fig. 1). In the North  
379 Pacific, the jet strengthening is slightly enhanced in PAT compared to UNI. At the same  
380 time, the pattern of SST increase has little or no impact on the jet strength response in  
381 the North Atlantic and on the jet latitude response in both ocean basins. In both ocean  
382 basins, about half to two-thirds of the poleward jet shift can be attributed to the cloud-  
383 radiative impact for UNI and PAT. In addition, the cloud-radiative impact contributes  
384 half to the jet strengthening in the North Atlantic for both UNI and PAT.

385 The above analysis shows that cloud-radiative changes contribute substantially to  
386 the circulation response independent of the pattern of surface warming, and that the cloud-  
387 radiative impact is nearly zonally symmetric. To understand this, Fig. 7 shows cloud cover  
388 changes and changes in cloud-radiative heating in the UNI and PAT simulations. The  
389 cloud cover changes and cloud-radiative heating changes are consistent with the verti-  
390 cal expansion of the troposphere and poleward expansion of the Tropics shown in Fig. 2,  
391 and with the fixed anvil temperature hypothesis, which states that high-level clouds rise  
392 in response to increased tropospheric temperatures to maintain their cloud-top temper-  
393 ature (Hartmann & Larson, 2002; Thompson et al., 2017). With high-level clouds warm-  
394 ing at their base and cooling at their top (see also Slingo & Slingo, 1988; Li & Thomp-  
395 son, 2016), the cloud rise leads to positive changes in cloud-radiative heating in the trop-  
396 ical and mid-latitude upper troposphere. The stronger tropical SST increase in PAT com-  
397 pared to UNI leads to a slightly larger change in cloud-radiative heating in the tropical  
398 upper-troposphere (Fig. S9), but overall the cloud-radiative heating change is very sim-  
399 ilar between UNI and PAT. A very similar pattern of cloud-radiative heating changes  
400 was previously found in aquaplanet simulations in which global warming was mimicked  
401 by a uniform 4 K SST increase (Fig. 2c, d in Voigt & Shaw, 2016), and in present-day sim-  
402 ulations in a slab ocean setup under quadrupling of atmospheric CO<sub>2</sub> (Fig. 2b of Voigt  
403 et al., 2019). Additionally, the pattern is consistent with the atmospheric cloud-radiative

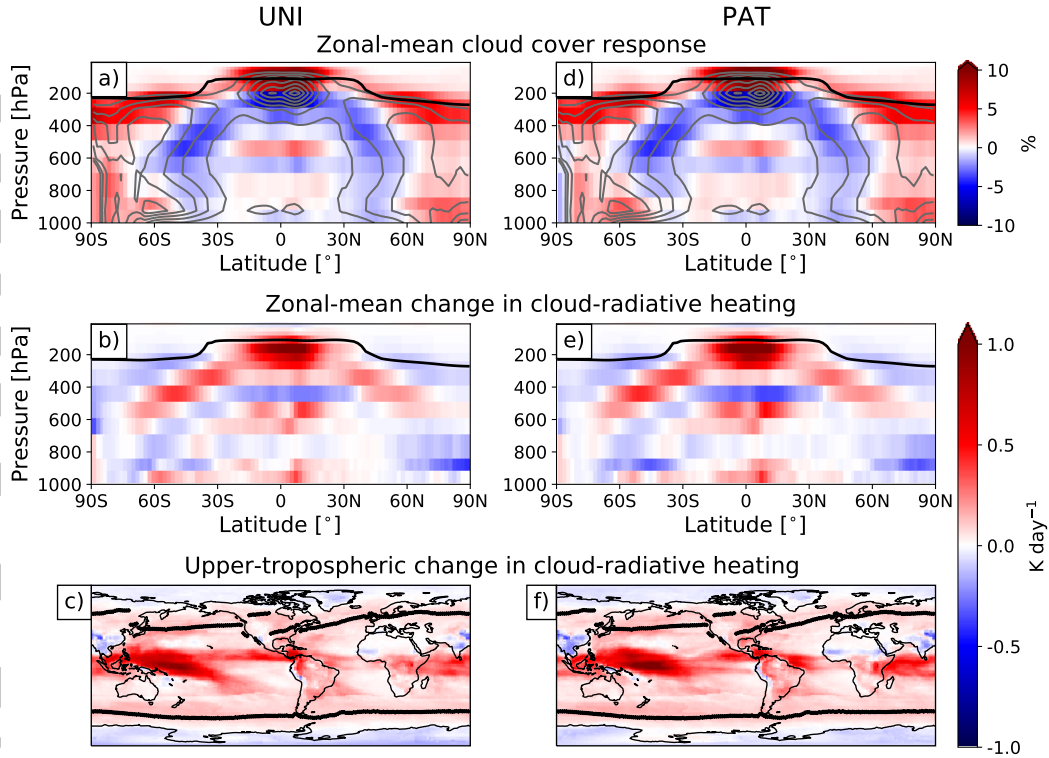


**Figure 7.** Annual-mean zonal-mean response of cloud cover in the simulations with free clouds (a, d) and annual-mean zonal-mean change in cloud-radiative heating (b, e). The bottom panels depict the vertical-mean changes in cloud-radiative heating for a 300 hPa thick layer below the tropopause. Results are shown for the UNI (left) and PAT (right) simulations. The black lines in the zonal-mean responses indicate the tropopause height in the control simulation, the black line in the maps shows the jet latitude in the control simulation.

404 heating changes derived from present-day COOKIE simulations (Fig. 4b in Li et al., 2019).

405 This supports the idea that the changes in cloud-radiative heating and, thus, the cloud-  
 406 radiative impact do not strongly depend on the details of surface warming.

407 Because our simulations include zonal asymmetries from continents, we further in-  
 408 vestigate the zonal structure of the changes in cloud-radiative heating. The largest changes  
 409 in cloud-radiative heating are located in the upper troposphere. We therefore analyze  
 410 the vertical-mean changes in cloud-radiative heating for a 300 hPa thick layer below the  
 411 tropopause (Fig. 7c, f). In the mid-latitudes of both hemispheres, the changes in cloud-  
 412 radiative heating are zonally symmetric and exhibit a similar magnitude in both global  
 413 warming setups (Fig. S9). This is consistent with the zonally symmetric cloud-radiative

414 impact in Fig. 4 and Fig. 5, which also exhibits similar magnitudes in both global warm-  
415 ing setups. Zonal asymmetries in the cloud-radiative heating changes are found in the  
416 Tropics, especially in the regions of deep convection over the western Pacific and the In-  
417 dian Ocean (Fig. 7c, f). This region also shows the largest change in cloud-radiative heat-  
418 ing. Because increased convection over this region can affect the jet latitude in the North  
419 Atlantic (e.g., Cassou, 2008; Henderson et al., 2016), we expect that the large change  
420 in cloud-radiative heating modifies the jet response in the North Atlantic. However, even  
421 though UNI and PAT exhibit different patterns of the upper-tropospheric change in cloud-  
422 radiative heating, the cloud-radiative impact on the North Atlantic jet stream response  
423 are similar in both global warming setups. This indicates that the small-scale structure  
424 of the change in cloud-radiative heating might be less important than its location in the  
425 western tropical Pacific.

#### 426 **4 Seasonal-mean circulation response**

427 In this section, we investigate the cloud-radiative impact on the seasonal-mean jet  
428 stream response and compare it to the annual-mean response. As in Section 3, we base  
429 our analysis on the total response in the prescribed-clouds setup and its decomposition  
430 into a cloud-radiative impact and an SST impact. To this end, Figs. 8-10 show the seasonal-  
431 mean wind and jet responses separately for each ocean basin. As for the annual-mean,  
432 an almost linear relationship between the poleward jet shift and jet strengthening is found  
433 in all three ocean basins during seasons which exhibit both the jet shift and jet strength-  
434 ening. The linear behavior is most strongly pronounced in the Southern Hemisphere dur-  
435 ing DJF and MAM.

436 As for the annual-mean, the seasonal-mean total zonal wind responses in UNI and  
437 PAT reproduce most of the robust zonal wind responses of the CMIP5 Amip4K and Amip-  
438 Future simulations (Figs. S4-S5, second to fifth rows). The largest differences compared  
439 to the robust response in the CMIP5 models occur in the North Pacific during DJF and  
440 MAM. In DJF, ICON does not reproduce the equatorward jet shift in the eastern part  
441 of the North Pacific. In MAM, ICON simulates a poleward shift in the North Pacific,  
442 whereas the CMIP5 models show a jet strengthening. In the Southern Hemisphere, ICON  
443 shows a jet strengthening east of South America in JJA and SON, whereas most of the  
444 CMIP5 models show a poleward shift in this region. The ocean basin mean jet responses  
445 in ICON are within the range of the CMIP5 models during most of the seasons and for

446 all three ocean basins (Figs. S6-S7), although ICON shows a comparably small poleward  
447 shift of the Southern Hemisphere jet in DJF and MAM, and little jet responses in JJA  
448 and SON, as well as a comparably large jet shift in the North Pacific during MAM.

449 In the North Atlantic, the cloud-radiative impact supports the poleward jet shift  
450 in UNI and PAT during all seasons (Fig. 8). It contributes to the jet strengthening in  
451 JJA and SON for the UNI simulations and during all seasons for the PAT simulations.  
452 With respect to the jet shift, the cloud-radiative impact exhibits only a small seasonal  
453 cycle and is of similar magnitude as in the annual-mean (compare Fig. 8 to top row of  
454 Fig. 6), except for MAM in the PAT simulations for reasons that are unknown to us. As  
455 in the annual-mean, and with the exception of MAM, the seasonal-mean cloud-radiative  
456 impact is largely independent of the SST pattern. In contrast, the total jet shift and the  
457 SST impact exhibit distinct seasonal cycles. This leads to strong seasonal variations of  
458 the relative importance of the cloud-radiative impact. The relative importance of the cloud-  
459 radiative impact can range from about a quarter (during DJF in PAT) to almost all of  
460 the poleward jet shift (during SON in PAT). With respect to the jet strength, the sea-  
461 sonal cycles of the total response, the cloud-radiative impact, and the SST impact are  
462 of similar magnitude. In the UNI simulations, the relative importance of the cloud-radiative  
463 impact on the jet strength varies between seasons. In the PAT simulations, more than  
464 three-quarter of the total jet strength response can be attributed to the cloud-radiative  
465 impact (except JJA).

466 In the North Pacific, the cloud-radiative impact leads to a poleward jet shift in all  
467 seasons, while having essentially no impact on the seasonal jet strength response (Fig. 9).  
468 Apart from JJA, the cloud-radiative impact on the jet latitude response is mostly inde-  
469 pendent of the SST pattern, consistent with the annual-mean response (Fig. 6, middle  
470 row). In terms of relative importance, the cloud-radiative impact contributes between  
471 about one-third to the jet shift during MAM, and is in fact larger than the total response  
472 during JJA. The strong seasonal cycle in the relative importance reflects the strong sea-  
473 sonal cycle of the SST impact, which contributes to a poleward jet shift in MAM but  
474 tends to lead to an equatorward shift in JJA. We note that the equatorward shift and  
475 weakening of the jet during JJA likely arises from negative land-sea equivalent poten-  
476 tial temperature contrasts when SST are warmed but atmospheric CO<sub>2</sub> is kept at the  
477 present-day level (Shaw & Voigt, 2015).

478 In the Southern Hemisphere, the four seasons can be arranged into two groups ac-  
 479 cording to the simulated jet shifts (Fig. 10). The first group consists of DJF and MAM,  
 480 for which the jet shifts poleward, similar to the annual-mean (compare Fig. 10 to lower  
 481 row of Fig. 6). The cloud-radiative impact is of similar magnitude during both seasons  
 482 and for both global warming setups. At the same time, the increased SST gradients in  
 483 PAT lead to a much stronger SST impact compared to UNI, so that the relative impor-  
 484 tance of the cloud-radiative impact ranges between about one-third (during DJF in PAT)  
 485 and more than half (during DJF in UNI) of the total jet shift. The second group con-  
 486 sists of SON and JJA, for which the total jet shift is small or even slightly equatorward,  
 487 independent of the pattern of SST increase. The slight equatorward shift during JJA is  
 488 supported by the cloud-radiative impact, while in SON, the jet latitude hardly responds

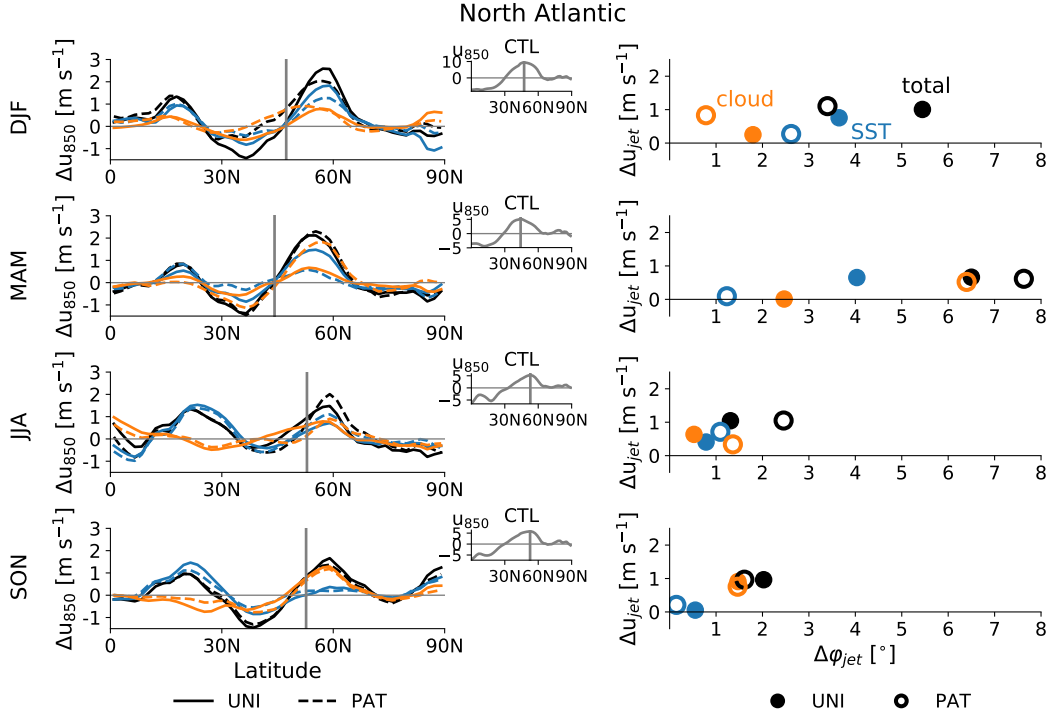


**Figure 8.** Seasonal-mean response of the ocean basin zonal-mean  $u_{850}$  response to a uniform (straight line) and patterned (dashed line) SST increase (left) in the North Atlantic. The grey bar indicates the jet latitude in the control simulation derived from the maximum in  $u_{850}$  (small inserted figures). The right panel shows the poleward jet shift  $\Delta\varphi_{jet}$  versus the jet strengthening  $\Delta u_{jet}$ . The total locked response (black) is decomposed into cloud-radiative impact (orange) and SST impact (blue).

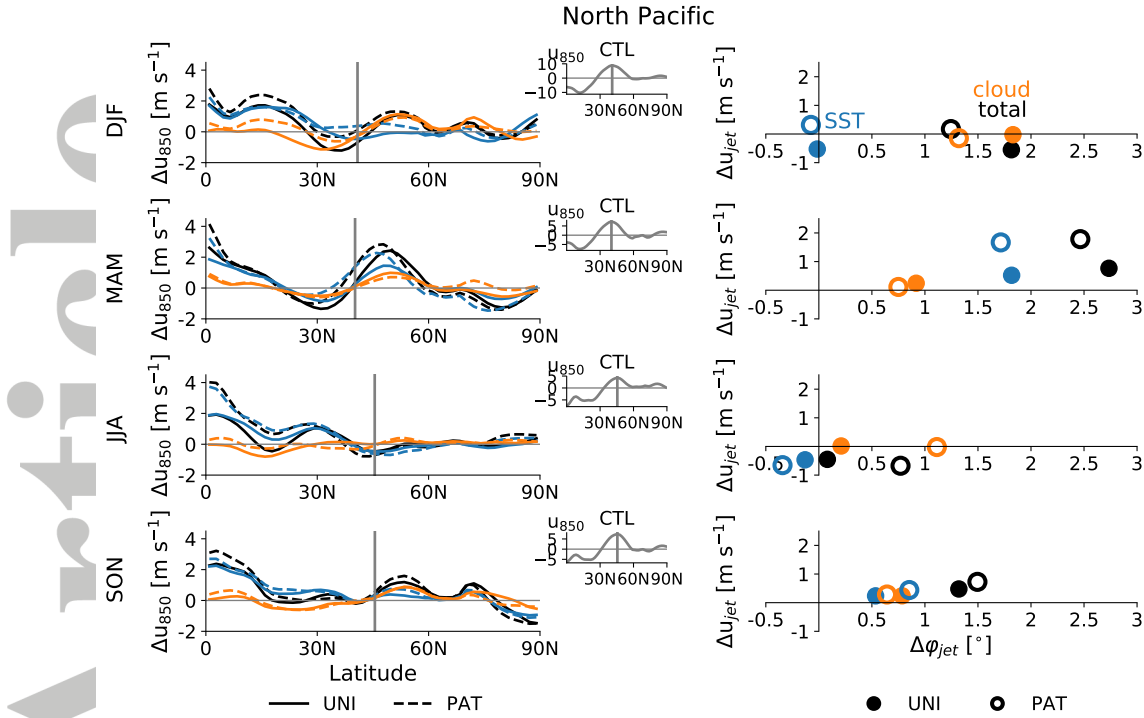


**Figure 9.** Same as Fig. 8, but for the North Pacific.

489 to global warming and the cloud-radiative impact is negligible. In contrast to seasonally-  
 490 dependent changes in its position, the jet becomes stronger in all four seasons. The cloud-  
 491 radiative impact on the jet strengthening is of similar magnitude during all seasons, and  
 492 its relative importance ranges between about one-fifth (during DJF and JJA in PAT)  
 493 and half (during SON in UNI) of the total response.

494 Figs. S10-S12 show maps of the seasonal-mean  $u_{850}$  responses in UNI and PAT, as  
 495 well as the differences between the two global warming setups. As for the annual-mean,  
 496 the seasonal-mean cloud-radiative impact is largely zonally symmetric in all ocean basins  
 497 and during most seasons, except for JJA. During this season, exceptions of the zonal cloud-  
 498 radiative impact are found in the North Pacific (in UNI), in the North Atlantic (in PAT)  
 499 and the Southern Hemisphere (in PAT). Note that during JJA, the cloud-radiative im-  
 500 pact is larger than the total jet shift in the North Pacific and counteracted by an almost  
 501 ocean basin wide equatorward shift due to the SST impact.

502 To sum up, we have shown that the seasonal-mean cloud-radiative impact is largely  
 503 zonally symmetric and shows little dependence on the pattern of SST increase during

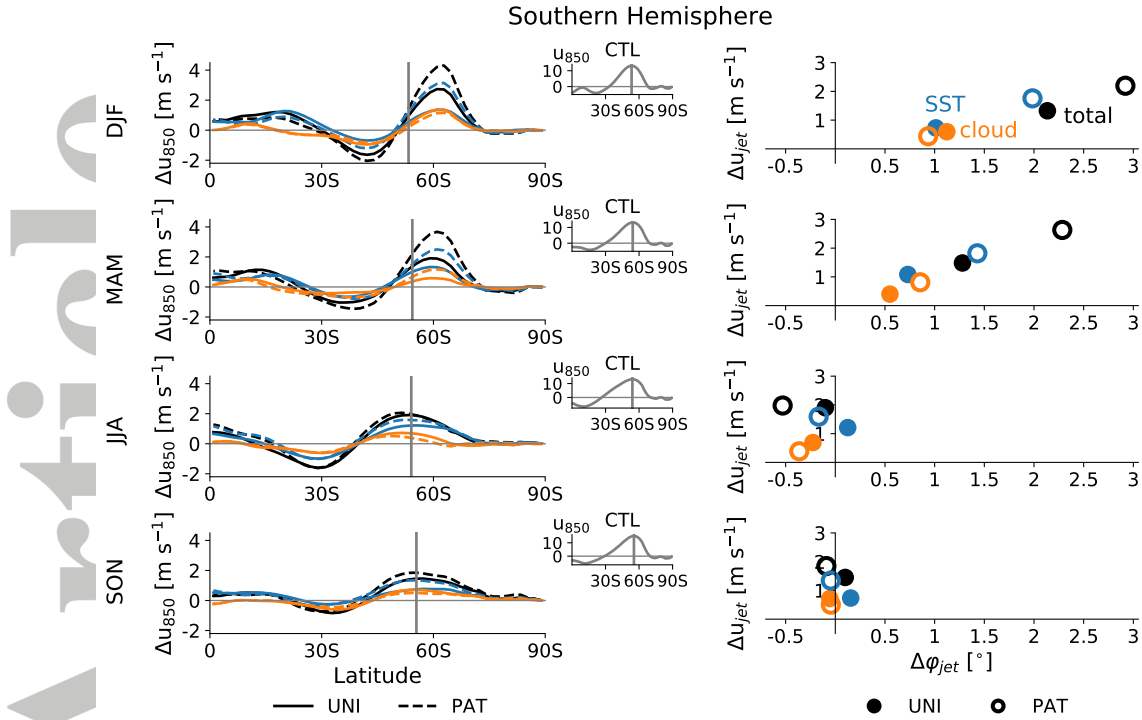


**Figure 10.** Same as Fig. 8, but for the Southern Hemisphere.

504 most seasons in all three ocean basins. In the North Atlantic and North Pacific, the cloud-  
 505 radiative impact varies little over the course of the year and supports the poleward jet  
 506 shift during all seasons. The relative importance of the cloud-radiative impact depends  
 507 on the season, because the total response and SST impact exhibit seasonal cycles. A sim-  
 508 ilar result is found for the Southern Hemisphere during DJF and MAM. The cloud-radiative  
 509 impact supports the jet strengthening in the North Atlantic during JJA and SON for  
 510 UNI and during all seasons for PAT, and contributes to the jet strengthening in the South-  
 511 ern Hemisphere during all seasons.

512 **5 Relations between the jet stream and the atmospheric equator-to-**  
 513 **pole temperature gradient**

514 In this section, we investigate to what extent the jet stream and its response to global  
 515 warming are correlated with the upper-tropospheric meridional temperature gradients  
 516 in all three ocean basins and all seasons. Following Harvey et al. (2014), we calculate  
 517 the upper-tropospheric (250 hPa) equator-to-pole temperature gradient as the difference  
 518 between ocean basin zonal mean tropical (30°S-30°N) and polar (poleward of 60°N/S)

519 atmospheric temperatures. We chose this pressure level because in our simulations the  
520 jet stream and the temperature gradient and their responses show higher correlations  
521 in the upper troposphere than in the lower troposphere.

522 In a first step, we investigate to what extent the annual-mean and seasonal-mean  
523 jet streams and upper-tropospheric temperature gradients are correlated for different states  
524 of the climate system. For this, we use the ocean basin mean jet latitude, jet strength  
525 and equator-to-pole temperature gradient of the seven simulations with locked clouds.  
526 These simulations are T1C1, T1C2, T2C1, T2C2, T1C3, T3C1 and T3C3. As described  
527 in Section 2.2, the numbers indicate whether SST (T) and cloud-radiative properties (C)  
528 are prescribed to values from CTL (simulation 1), UNI (simulation 2) or PAT (simula-  
529 tion 3). Fig. S13 shows the scatter plots from which the correlation coefficients of Tab. 1  
530 were derived. The seven simulations are not strongly clustered according to the under-  
531 lying SST pattern during most seasons and for most of the ocean basins. Thus, the sig-  
532 nificant correlations between the temperature gradient and jet stream are not driven by  
533 the SST increase. In the Southern Hemisphere, the jet latitude and jet strength are sig-  
534 nificantly correlated with the upper-tropospheric temperature gradient both in the annual-  
535 mean and in most seasons (except for JJA and SON for the jet latitude) (Tab. 1). In the  
536 North Pacific, the jet stream is significantly correlated with the temperature gradient  
537 during MAM and SON. Note that in both ocean basins negative correlations between  
538 the temperature gradient and jet latitude or jet strength are found, and are significant  
539 in the North Pacific during JJA. The negative correlation during JJA is consistent with  
540 the findings of Shaw & Voigt (2015), who showed that ocean warming can result in an  
541 equatorward shift of the North Pacific jet in summer. The North Atlantic jet stream is  
542 not significantly correlated with the temperature gradient during most seasons. In sum-  
543 mary, our results indicate that the upper-tropospheric temperature gradient bears some  
544 information for the position and strength of the Southern Hemisphere jet stream, but  
545 little information for the North Pacific and North Atlantic jet streams.

546 Previous studies related the global warming response of the mid-latitude circula-  
547 tion to changes in upper- and/or lower-tropospheric meridional temperature gradients  
548 (e.g., Yin, 2005; Lorenz & DeWeaver, 2007; Harvey et al., 2014, 2015). Thus, in a sec-  
549 ond step, we investigate whether the cloud-radiative impact on the temperature gradi-  
550 ent response in the three ocean basins can be used to infer the cloud-radiative impact  
551 on the jet stream response in the respective ocean basin. The idea for this originated from

**Table 1.** Correlation coefficients for linear correlation between ocean basin mean jet latitude and upper-tropospheric temperature gradient (a). Panel b shows the same for the jet strength. Correlation coefficients which are significant at a 95 % level are shown in bold letters for better visualization of large linear correlations. Positive correlations indicate that increased (decreased) temperature gradients correspond to (a) a more poleward (equatorward) located and (b) a stronger (weaker) jet stream.

a)	Jet latitude		
	North Atlantic	North Pacific	Southern Hemisphere
Annual-mean	<b>0.87</b>	0.74	<b>0.95</b>
DJF	0.71	0.19	<b>0.96</b>
MAM	0.66	<b>0.97</b>	<b>0.87</b>
JJA	0.75	-0.09	-0.37
SON	0.58	<b>0.92</b>	0.18
b)	Jet strength		
	North Atlantic	North Pacific	Southern Hemisphere
Annual-mean	0.76	0.76	<b>0.96</b>
DJF	0.63	-0.04	<b>0.90</b>
MAM	0.45	<b>0.81</b>	<b>0.93</b>
JJA	<b>0.89</b>	<b>-0.89</b>	<b>0.96</b>
SON	0.58	<b>0.90</b>	<b>0.97</b>

552 the work of Gerber & Son (2014) who related, and thereby attributed, the jet shift to  
553 changes in polar stratospheric temperatures (due to ozone) and changes in tropical upper-  
554 tropospheric temperatures (due to greenhouse gases). A similar approach was taken by  
555 Ceppi & Shepherd (2017). Here, we investigate the relation between the jet response and  
556 the temperature gradient response for the SST impact and the cloud-radiative impact.  
557 The correlation between the jet stream response and the equator-to-pole temperature  
558 gradient response at 250 hPa is shown in Fig. 11. In all three ocean basins, the temper-  
559 ature gradient increases in response to global warming in all seasons (Fig. 11). At the  
560 same time, the jet strengthens and shifts poleward in the North Atlantic, and strength-  
561 ens in the Southern Hemisphere during all seasons. However, as discussed in Section 4,  
562 during some seasons, the North Pacific jet stream weakens and shifts equatorward and  
563 the Southern Hemisphere jet stream shifts equatorward.

564 To assess to what extent the temperature gradient response and the jet stream re-  
565 sponse are correlated, we calculate correlation coefficients individually for the total re-  
566 sponse, SST impact and cloud-radiative impact based on the annual-mean and seasonal-  
567 mean responses in both UNI and PAT. The cloud-radiative impact shows rather small  
568 correlations, except for the jet shift in the Southern Hemisphere (Fig. 11). This is due  
569 to the fact that the cloud-radiative impact is of similar magnitude over the course of the  
570 year and for both global warming simulations. In contrast, the total response and SST  
571 impact exhibit distinct seasonal cycles, resulting in significant correlations between the  
572 jet response and the temperature gradient response, especially in the Southern Hemi-  
573 sphere and North Pacific. This suggests that in a large model ensemble for which only  
574 the total response is available, such as CMIP5/6, the SST impact could be inferred in-  
575 directly from the upper-tropospheric temperature response, but the cloud-radiative im-  
576 pact could not. Thus, a proper diagnostic of the cloud-radiative impact requires dedi-  
577 cated cloud-locking simulations.

578 The fact that we generally could not find a linear correlation for the cloud-radiative  
579 impact is in agreement with McGraw & Barnes (2016), who used a dry dynamical model  
580 to investigate the jet stream response to a time-constant tropical upper-tropospheric ther-  
581 mal forcing. They found that the temperature response to the thermal forcing does not  
582 exhibit a seasonal cycle, whereas, the jet latitude and jet strength responses do exhibit  
583 distinct seasonal cycles. As a result, McGraw & Barnes (2016) found no correlation be-

Accepted Article

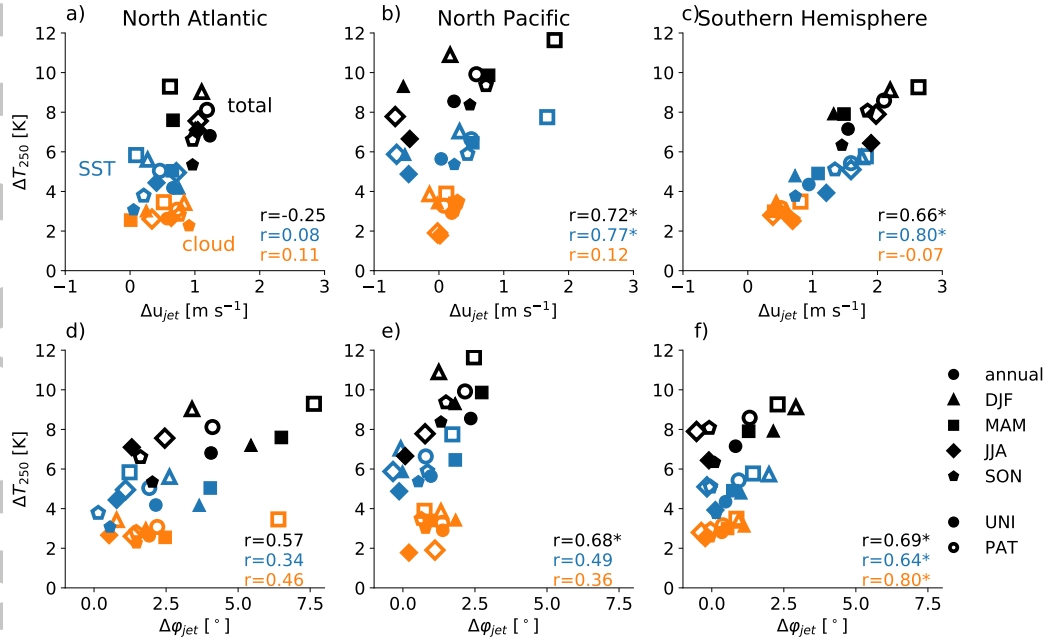


**Figure 11.** Correlation between temperature gradient response at 250 hPa,  $\Delta T_{250}$ , and jet strength response,  $\Delta u_{jet}$ , (top) and jet latitude response,  $\Delta \varphi_{jet}$ , (bottom) for the North Atlantic, North Pacific and Southern Hemisphere. Filled markers are for the response in UNI, open markers for the response in PAT. The total response (black markers) is decomposed into the cloud-radiative impact (orange markers) and the SST impact (blue markers). Correlation coefficients  $r$  are marked with a star if they are significant on a 95 % level.

584 tween the jet stream response and the temperature gradient response. This is in line with  
585 our results.

## 586 **6 Discussion and Conclusions**

587 We study the impact of cloud-radiative changes on the global warming responses  
588 of the mid-latitude jet streams and storm tracks in the North Atlantic, North Pacific and  
589 Southern Hemisphere, and determine whether the cloud-radiative impact depends on the  
590 ocean basin, season and pattern of SST increase. For this purpose, we use the atmospheric  
591 component of the ICON model and prescribe SST to isolate the impact of cloud-radiative  
592 changes via the atmospheric pathway, i.e., the impact of changes in atmospheric cloud-  
593 radiative heating in the absence of a cloud-radiative impact on ocean surface temper-  
594 atures (Voigt et al., 2019).

595 Changes in atmospheric cloud-radiative heating have a substantial impact on the  
596 annual-mean jet stream and storm track responses to global warming, with little depen-  
597 dence on the pattern of SST increase. Note that the impact of surface cloud-radiative  
598 heating, which is disabled in our simulations, may depend on the pattern of SST increase,  
599 because they lead to changes in surface temperatures (Ceppi & Hartmann, 2016; Voigt  
600 et al., 2019). The cloud-radiative impact is largely zonally symmetric, consistent with  
601 a zonally symmetric change in cloud-radiative heating in the mid-latitude upper tropo-  
602 sphere. The magnitude of the cloud-radiative impact depends on the ocean basin. In a  
603 relative sense, cloud-radiative changes contribute one- to two-thirds to the annual-mean  
604 poleward jet shift in all three ocean basins, and support the jet strengthening in the North  
605 Atlantic and Southern Hemisphere. Regarding the seasonal jet response, the cloud-radiative  
606 impact varies little with seasons in the North Atlantic and North Pacific. Yet, because  
607 the total jet stream response and the SST impact exhibit distinct seasonal cycles, the  
608 relative importance of the cloud-radiative impact changes over the course of the year.  
609 In the Southern Hemisphere, the cloud-radiative impact supports the jet strengthening  
610 in all seasons and contributes to the poleward jet shift in austral summer and fall. As  
611 for the annual-mean, the cloud-radiative impact on the seasonal jet stream response is  
612 largely zonally symmetric and depends little on the pattern of SST increase.

613 Similar to the zonal cloud-radiative impact, the direct radiative impact of CO<sub>2</sub> on  
614 the zonal wind response is also largely zonally uniform in present-day simulations of at-

615 atmospheric general circulation models (Grise & Polvani, 2014a). Grise & Polvani (2014a)  
616 also attributed the asymmetries in the total response to changes in the SST, as in our  
617 study with the cloud-locking method.

618 Previous studies investigated the zonal-mean jet stream and storm track responses  
619 to global warming in idealized aquaplanet simulations without a seasonal cycle. They  
620 found that cloud-radiative changes cause more than half of the zonal-mean near-surface  
621 zonal wind (Voigt & Shaw, 2015) and jet latitude responses (Ceppi & Hartmann, 2016)  
622 and dominate the storm track response (Ceppi & Hartmann, 2016). Voigt et al. (2019)  
623 showed that more than half of the annual-mean zonal-mean jet shift in a present-day setup  
624 can be attributed to the atmospheric pathway of the cloud-radiative impact. We extend  
625 this prior work and show that the absolute value of the cloud-radiative impact strongly  
626 depends on the ocean basin, and has only a small seasonal cycle in the Northern Hemi-  
627 sphere. In addition, we show that the relative role of the cloud-radiative impact on the  
628 jet stream response varies across ocean basins and seasons. This highlights the impor-  
629 tance of the present-day setup, and the investigation of individual ocean basins, for un-  
630 derstanding the role of cloud-radiative changes on the mid-latitude circulation response  
631 to global warming.

632 While continents are important for the jet stream response in the three ocean basins,  
633 the pattern of SST increase plays a minor role for the cloud-radiative impact on the jet  
634 stream and storm track responses. In our simulations, the pattern of the SST increase  
635 has only a small impact on the absolute value of the cloud-radiative impact in all three  
636 ocean basins and across seasons. Thus, the uniform 4 K SST increase provides meaning-  
637 ful estimates of the absolute value of the cloud-radiative impact, although is not able to  
638 reproduce the total jet stream response of coupled climate models, especially in the South-  
639 ern Hemisphere, where the jet strongly responds to changes in SST gradients.

640 Even though the cloud-radiative impact does not strongly depend on the pattern  
641 of SST increase and season in the model used here, previous work indicates that the cloud-  
642 radiative impact strongly differs between models. Voigt et al. (2019) showed that the annual-  
643 mean zonal-mean change in atmospheric cloud-radiative heating and, thus, the magni-  
644 tude of the cloud-radiative impact strongly depend on the model. These model differ-  
645 ences arise both from differences in the cloud response as well as differences in the ra-  
646 diation schemes and assumptions regarding the radiative characteristics of ice clouds.

647 Additionally, in coupled climate models the cloud-radiative impact is a sum of the at-  
648 mospheric and surface pathways of the change in cloud-radiative heating. The latter might  
649 depend on the pattern of SST increase and season.

650 Finally, we investigated the correlation between the upper-tropospheric temper-  
651 ature gradient response and the jet stream response. For the cloud-radiative impact, in-  
652 creased temperature gradients coincide with a strengthening of the Southern Hemisphere  
653 jet stream, while correlations between cloud-induced changes in the temperature gradi-  
654 ent and the jet are weak in the Northern Hemisphere. This lack of correlation is a re-  
655 sult of the fact that the cloud-radiative impact does not strongly depend on season in  
656 the Northern Hemisphere. In contrast, the total response and SST impact exhibit dis-  
657 tinct seasonal cycles, resulting in significant linear correlations between the jet stream  
658 response and upper-tropospheric temperature gradient response, with statistically sig-  
659 nificant correlations in the Southern Hemisphere and North Pacific. This also indicates  
660 that the cloud-radiative impact on the jet cannot be inferred indirectly from the tem-  
661 perature response, but requires cloud-locking simulations.

662 Our results emphasize the importance of cloud-radiative changes for the global warm-  
663 ing response of the mid-latitude atmospheric circulation. Previous studies, which focused  
664 on the annual-mean zonal-mean cloud-radiative impact, showed that its magnitude dif-  
665 fers across models and remains uncertain in both aquaplanet (Voigt & Shaw, 2016) and  
666 present-day simulations (Voigt et al., 2019). Thus, future studies should investigate the  
667 ocean basin mean circulation response across seasons in a larger model ensemble. This  
668 would enable to quantify model differences in representing the change in cloud-radiative  
669 heating and its effect on the circulation’s response. Finally, we found a particularly large  
670 change in cloud-radiative heating over the tropical western Pacific and Indian Ocean, which  
671 could be important for the mid-latitude circulation response to global warming. We hope  
672 to quantify the role of this heating in a future study using regionally prescribed cloud-  
673 radiative changes.

#### 674 **Acknowledgments**

675 N.A. and A.V. are supported by the German Ministry of Education and Research (BMBF)  
676 and FONA: Research for Sustainable Development ([www.fona.de](http://www.fona.de)) under grant agreement  
677 01LK1509A. J.G.P. thanks AXA research fund for support. The ICON simulations were  
678 carried out by N.A. and A.V. at the Mistral supercomputer of the German Climate Com-

679 puting Center (DKRZ) in Hamburg, Germany, and are published at KITopen with doi  
 680 10.5445/IR/1000094317. This work contributes to the WCRP’s Grand Challenge on Clouds,  
 681 Circulation, and Climate Sensitivity and the BMBF-funded project “HD(CP)<sup>2</sup>: High Def-  
 682 inition Clouds and Precipitation for Advancing Climate Prediction”.

## 683 References

- 684 Allan, R. P. (2011). Combining satellite data and models to estimate cloud radiative  
 685 effect at the surface and in the atmosphere. *Met. Apps.*, *18*(3), 324–333. doi: 10  
 686 .1002/met.285
- 687 Barnes, E. A., & Polvani, L. M. (2013). Response of the midlatitude jets and of  
 688 their variability to increased greenhouse gases in CMIP5 models. *J. Climate*, *26*,  
 689 7117–7135.
- 690 Blackmon, M. L. (1976). A Climatological Spectral Study of the 500 mb Geopoten-  
 691 tial Height of the Northern Hemisphere. *J. Atmos. Sci.*, *33*(8), 1607–1623. doi: 10  
 692 .1175/1520-0469(1976)033<1607:ACSSOT>2.0.CO;2
- 693 Bony, S., Stevens, B., Frierson, D. M. W., Jakob, C., Kageyama, M., Pincus, R., ...  
 694 Webb, M. J. (2015). Clouds, circulation and climate sensitivity. *Nature Geosci.*,  
 695 *8*, 261–268. doi: 10.1038/ngeo2398
- 696 Brayshaw, D. J., Hoskins, B. J., & Blackburn, M. (2009). The basic ingredients  
 697 of the North Atlantic storm track. Part I: land-sea contrast and orography. *J. At-  
 698 mos. Sci.*, *66*(9), 2539–2558. doi: 10.1175/2009JAS3078.1
- 699 Butler, A. H., Thompson, D. W., & Heikes, R. (2010). The Steady-State At-  
 700 mospheric Circulation Response to Climate Change-like Thermal Forcings  
 701 in a Simple General Circulation Model. *J. Climate*, *23*, 3474–3496. doi:  
 702 10.1175/2010JCLI3228.1
- 703 Cassou, C. (2008). Intraseasonal interaction between the Madden–Julian oscillation  
 704 and the North Atlantic Oscillation. *Nature*, *455*(7212), 523–527. doi: 10.1038/  
 705 nature07286
- 706 Ceppi, P., & Hartmann, D. L. (2016). Clouds and the atmospheric circulation re-  
 707 sponse to warming. *J. Climate*, *29*, 783–799. doi: 10.1175/JCLI-D-15-0394.1
- 708 Ceppi, P., Hwang, Y.-T., Frierson, D. M. W., & Hartmann, D. L. (2012). Southern  
 709 Hemisphere jet latitude biases in CMIP5 models linked to shortwave cloud forcing.  
 710 *Geophys. Res. Lett.*, *39*, L19708. doi: 10.1029/2012GL053115

- 711 Ceppi, P., & Shepherd, T. G. (2017). Contributions of Climate Feedbacks to  
 712 Changes in Atmospheric Circulation. *J. Climate*, *30*(22), 9097-9118. doi:  
 713 10.1175/JCLI-D-17-0189.1
- 714 Ceppi, P., Zappa, G., Shepherd, T. G., & Gregory, J. M. (2018). Fast and Slow  
 715 Components of the Extratropical Atmospheric Circulation Response to CO<sub>2</sub> Forc-  
 716 ing. *J. Climate*, *31*(3), 1091-1105. doi: 10.1175/JCLI-D-17-0323.1
- 717 Ceppi, P., Zelinka, M. D., & Hartmann, D. L. (2014). The Response of the South-  
 718 ern Hemispheric Eddy-Driven Jet to Future Changes in Shortwave Radiation in  
 719 CMIP5. *Geophys. Res. Lett.*, *41*, 3244-3250. doi: 10.1002/2014GL060043
- 720 Chang, E. K. M., Guo, Y., & Xia, X. (2012). CMIP5 multimodel ensemble projec-  
 721 tion of storm track change under global warming. *J. Geophys. Res.*, *117*(D23118).  
 722 doi: 10.1029/2012JD018578
- 723 Chang, E. K. M., Lee, S., & Swanson, K. L. (2002). Storm Track Dynamics. *J. Cli-  
 724 mate*, *15*(16), 2163-2183. doi: 10.1175/1520-0442(2002)015<02163:STD>2.0.CO;2
- 725 Christoph, M., Ulbrich, U., & Haak, U. (1995). Faster Determination of the In-  
 726 traseasonal Variability of Storm Tracks Using Murakami's Recursive Filter. *Mon.  
 727 Weather Rev.*, *123*(2), 578-581. doi: 10.1175/1520-0493(1995)123<0578:FDOTIV>2  
 728 .0.CO;2
- 729 Gates, W. L. (1992). AMIP: The Atmospheric Model Intercomparison Project. *B.  
 730 Am. Meteorol. Soc.*, *73*(12), 1962-1970. doi: 10.1175/1520-0477(1992)073<1962:  
 731 ATAMIP>2.0.CO;2
- 732 Gerber, E. P., & Son, S.-W. (2014). Quantifying the Summertime Response of  
 733 the Austral Jet Stream and Hadley Cell to Stratospheric Ozone and Greenhouse  
 734 Gases. *J. Climate*, *27*, 5538-5559. doi: 10.1175/JCLI-D-13-00539.1
- 735 Grise, K. M., & Polvani, L. M. (2014a). The response of midlatitude jets to in-  
 736 creased CO<sub>2</sub>: Distinguishing the roles of sea surface temperature and direct radia-  
 737 tive forcing. *Geophys. Res. Lett.*, *41*(19), 6863-6871. doi: 10.1002/2014GL061638
- 738 Grise, K. M., & Polvani, L. M. (2014b). Southern Hemisphere cloud-dynamics bi-  
 739 ases in CMIP5 models and their implications for climate projections. *J. Climate*,  
 740 *27*, 6074-6092. doi: <http://dx.doi.org/10.1175/JCLI-D-14-00113.1>
- 741 Hartmann, D. L., & Larson, K. (2002). An important constraint on tropical cloud -  
 742 climate feedback. *Geophys. Res. Lett.*, *29*(20), 1951. doi: 10.1029/2002GL015835
- 743 Harvey, B. J., Shaffrey, L. C., & Woollings, T. J. (2014). Equator-to-pole tempera-

- 744 ture differences and the extra-tropical storm track responses of the CMIP5 climate  
 745 models. *Clim. Dyn.*, *43*(5), 1171–1182. doi: 10.1007/s00382-013-1883-9
- 746 Harvey, B. J., Shaffrey, L. C., & Woollings, T. J. (2015). Deconstructing the climate  
 747 change response of the Northern Hemisphere wintertime storm tracks. *Clim. Dyn.*,  
 748 *45*(9), 2847–2860. Retrieved from [https://doi.org/10.1007/s00382-015-2510-](https://doi.org/10.1007/s00382-015-2510-8)  
 749 [8](https://doi.org/10.1007/s00382-015-2510-8) doi: 10.1007/s00382-015-2510-8
- 750 Henderson, S., D. Maloney, E., & Barnes, E. (2016). The Influence of the Madden-  
 751 Julian Oscillation on Northern Hemisphere Winter Blocking. *J. Climate*, *29*,  
 752 4597–4616. doi: 10.1175/JCLI-D-15-0502.1
- 753 Hollingsworth, A., Engelen, R. J., Textor, C., Benedetti, A., Boucher, O., Cheval-  
 754 lier, F., ... the GEMS Consortium (2008). TOWARD A MONITORING AND  
 755 FORECASTING SYSTEM FOR ATMOSPHERIC COMPOSITION. *Bull. Amer.*  
 756 *Meteor. Soc.*, *89*(8), 1147–1164. doi: 10.1175/2008BAMS2355.1
- 757 Hoskins, B. J., & Valdes, P. J. (1990). On the Existence of Storm-Tracks. *J. Atmos.*  
 758 *Sci.*, *47*(15), 1854–1864. doi: 10.1175/1520-0469(1990)047<1854:OTEOST>2.0.CO;  
 759 2
- 760 Kushner, P. J., Held, I. M., & Delworth, T. L. (2001). Southern Hemisphere at-  
 761 mospheric circulation response to global warming. *J. Climate*, *14*(10), 2238–2249.  
 762 doi: 10.1175/1520-0442(2001)014<0001:SHACRT>2.0.CO;2
- 763 Langen, P. L., Graversen, R. G., & Mauritsen, T. (2012). Separation of Contribu-  
 764 tions from Radiative Feedbacks to Polar Amplification on an Aquaplanet. *J. Cli-*  
 765 *mate*, *25*(8), 3010–3024.
- 766 Li, Y., & Thompson, D. W. J. (2016). Observed Signatures of the Barotropic  
 767 and Baroclinic Annular Modes in Cloud Vertical Structure and Cloud Radiative  
 768 Effects. *J. Climate*, *29*(13), 4723–4740. doi: 10.1175/JCLI-D-15-0692.1
- 769 Li, Y., Thompson, D. W. J., & Bony, S. (2015). The Influence of Atmospheric Cloud  
 770 Radiative Effects on the Large-Scale Atmospheric Circulation. *J. Climate*, *8*,  
 771 7263–7278. doi: 10.1175/JCLI-D-14-00825.1
- 772 Li, Y., Thompson, D. W. J., Bony, S., & Merlis, T. M. (2019). Thermodynamic  
 773 Control on the Poleward Shift of the Extratropical Jet in Climate Change Simu-  
 774 lations: The Role of Rising High Clouds and Their Radiative Effects. *J. Climate*,  
 775 *32*, 917–934. doi: 10.1175/JCLI-D-18-0417.1
- 776 Lorenz, D. J., & DeWeaver, E. T. (2007). Tropopause height and zonal wind re-

- 777        sponse to global warming in the ipcc scenario integrations. *J. Geophys. Res.*, *112*,  
778        D10119. doi: 10.1029/2006JD008087
- 779        Lu, J., Chen, G., & Frierson, D. M. W. (2008). Response of the Zonal Mean Atmo-  
780        spheric Circulation to El Nio versus Global Warming. *J. Climate*, *21*(22), 5835–  
781        5851. doi: 10.1175/2008JCLI2200.1
- 782        Ma, J., & Xie, S.-P. (2013). Regional Patterns of Sea Surface Temperature Change:  
783        A Source of Uncertainty in Future Projections of Precipitation and Atmospheric  
784        Circulation. *J. Climate*, *26*(8), 2482–2501. doi: 10.1175/JCLI-D-12-00283.1
- 785        Mauritsen, T., Graversen, R. G., Klocke, D., Langen, P. L., Stevens, B., &  
786        Tomassini, L. (2013). Climate feedback efficiency and synergy. *Clim. Dyn.*,  
787        *41*, 2539–2554. doi: 10.1007/s00382-013-1808-7
- 788        McGraw, M. C., & Barnes, E. A. (2016). Seasonal Sensitivity of the Eddy-Driven  
789        Jet to Tropospheric Heating in an Idealized AGCM. *J. Climate*, *29*(14), 5223–  
790        5240. doi: 10.1175/JCLI-D-15-0723.1
- 791        Pinto, J. G., Spanghel, T., Ulbrich, U., & Speth, P. (2006). Assessment of winter  
792        cyclone activity in a transient ECHAM4-OPYC3 GHG experiment. *Meteorol. Z.*,  
793        *15*(3), 279–291. doi: 10.1127/0941-2948/2006/0128
- 794        Pinto, J. G., Ulbrich, U., Leckebusch, G. C., Spanghel, T., Reyers, M., & Zacharias,  
795        S. (2007). Changes in storm track and cyclone activity in three SRES ensemble  
796        experiments with the ECHAM5/MPI-OM1 GCM. *Clim. Dyn.*, *29*(2), 195–210.  
797        doi: 10.1007/s00382-007-0230-4
- 798        Polvani, L. M., Waugh, D. W., Correa, G. J. P., & Son, S.-W. (2011). Strato-  
799        spheric Ozone Depletion: The Main Driver of Twentieth-Century Atmospheric  
800        Circulation Changes in the Southern Hemisphere. *J. Climate*, *24*, 795–812. doi:  
801        10.1175/2010JCLI3772.1
- 802        Schneider, E. K., Kirtman, B. P., & Lindzen, R. S. (1999). Tropospheric Water Va-  
803        por and Climate Sensitivity. *J. Atmos. Sci.*, *56*(11), 1649–1658. doi: 10.1175/1520-  
804        -0469(1999)056<1649:TWVACS>2.0.CO;2
- 805        Shaw, T. A., Baldwin, M., Barnes, E. A., Caballero, R., Garfinkel, C. I., Hwang,  
806        Y.-T., ... Voigt, A. (2016). Storm track processes and the opposing influences of  
807        climate change. *Nature Geosci.*, *9*. doi: 10.1038/ngeo2783
- 808        Shaw, T. A., & Voigt, A. (2015). Tug of war on summertime circulation between ra-  
809        diative forcing and sea surface warming. *Nature Geosci.*, *8*, 560–566. doi: 10.1038/

810 ngeo2449

811 Shepherd, T. G. (2014). Atmospheric circulation as a source of uncertainty in cli-  
812 mate change projections. *Nature Geosci.*, 7, 703-708. doi: 10.1038/ngeo2253

813 Simpson, I. R., Shaw, T. A., & Seager, R. (2014). A Diagnosis of the Seasonally and  
814 Longitudinally Varying Midlatitude Circulation Response to Global Warming. *J.*  
815 *Atmos. Sci.*, 71, 2489-2515. doi: <http://dx.doi.org/10.1175/JAS-D-13-0325.1>

816 Slingo, A., & Slingo, J. M. (1988). The response of a general-circulation model to  
817 cloud longwave radiative forcing. Part I: Introduction and initial experiments. *Q.*  
818 *J. R. Meteorol. Soc.*, 114, 1027-1062. doi: 10.1002/qj.49711448209

819 Stevens, B., Bony, S., & Webb, M. (2012). Clouds On-Off Klimate Intercomparion  
820 Experiment (COOKIE)., available at <http://www.euclipse.eu/wp4/wp4.html>.

821 Taylor, K. E., Stouffer, R. J., & Meehl, G. A. (2009). A Summary of the CMIP5 Ex-  
822 periment Design. *PCMDI Reports*. Retrieved from [https://pcmdi.llnl.gov/](https://pcmdi.llnl.gov/mips/cmip5/experiment_design.html)  
823 [mips/cmip5/experiment\\_design.html](https://pcmdi.llnl.gov/mips/cmip5/experiment_design.html)

824 Taylor, K. E., Stouffer, R. J., & Meehl, G. A. (2012). An Overview of CMIP5 and  
825 the Experiment Design. *Bull. Amer. Meteor. Soc.*, 93, 485-498. doi: 10.1175/  
826 BAMS-D-11-00094.1

827 Tegen, I., Hollrig, P., Chin, M., Fung, I., Jacob, D., & Penner, J. (1997). Contribu-  
828 tion of different aerosol species to the global aerosol extinction optical thickness:  
829 Estimates from model results. *J. Geophys. Res.*, 102(D20), 23895-23915. doi:  
830 10.1029/97JD01864

831 Thompson, D. W. J., Bony, S., & Li, Y. (2017). Thermodynamic constraint on the  
832 depth of the global tropospheric circulation. *PNAS*, 114(31), 8181-8186. doi: 10  
833 .1073/pnas.1620493114

834 Ulbrich, U., Leckebusch, G. C., & Pinto, J. G. (2009). "Extra-tropical cyclones in  
835 the present and future climate: a review. *Theor. Appl. Climatol.*, 96(1), 117-131.  
836 doi: 10.1007/s00704-008-0083-8

837 Ulbrich, U., Pinto, J. G., Kupfer, H., Leckebusch, G. C., Spangehl, T., & Rey-  
838 ers, M. (2008). Changing Northern Hemisphere Storm Tracks in an Ense-  
839 mble of IPCC Climate Change Simulations. *J. Climate*, 21(8), 1669-1679. doi:  
840 10.1175/2007JCLI1992.1

841 Vallis, G. K., Zurita-Gotor, P., Cairns, C., & Kidston, J. (2015). Response of the  
842 large-scale structure of the atmosphere to global warming. *Q. J. R. Meteorol.*

- 843 *Soc.*, 141, 1479-1501. doi: 10.1002/qj.2456
- 844 Vavrus, S. J. (2018). The influence of arctic amplification on mid-latitude weather  
845 and climate. *Current Climate Change Reports*. doi: 10.1007/s40641-018-0105-2
- 846 Voigt, A., Albern, N., & Papavasileiou, G. (2019). The atmospheric pathway of the  
847 cloud-radiative impact on the circulation response to global warming: important  
848 and uncertain. *J. Climate (in press)*. doi: 10.1175/JCLI-D-18-0810.1
- 849 Voigt, A., & Shaw, T. A. (2015). Circulation response to warming shaped by radia-  
850 tive changes of clouds and water vapor. *Nature Geosci.*, 8, 102-106. doi: 10.1038/  
851 ngeo2345
- 852 Voigt, A., & Shaw, T. A. (2016). Impact of regional atmospheric cloud-radiative  
853 changes on shifts of the extratropical jet stream in response to global warming. *J.*  
854 *Climate*, 29(23), 8399-8421. doi: 10.1175/JCLI-D-16-0140.1
- 855 Wetherald, R. T., & Manabe, S. (1988). Cloud Feedback Processes in a General Cir-  
856 culation Model. *J. Atmos. Sci.*, 45(8), 1397-1416.
- 857 Woollings, T., Gregory, J. M., Pinto, J. G., Meyers, M., & Brayshaw, D. J. (2012).  
858 Response of the North Atlantic storm track to climate change shaped by ocean-at-  
859 mosphere coupling. *Nature Geosci.*, 5, 313-317. doi: 10.1038/ngeo1438
- 860 Yin, J. H. (2005). A consistent poleward shift of the storm tracks in simulations of  
861 21st century climate. *Geophys. Res. Lett.*, 32, L18701.
- 862 Zängl, G., Reinert, D., Ripodas, P., & Baldauf, M. (2015). The ICON (ICOsahe-  
863 dral Non-hydrostatic) modelling framework of DWD and MPI-M: Description of  
864 the non-hydrostatic dynamical core. *Q. J. R. Meteorol. Soc.*, 141, 563-579. doi:  
865 10.1002/qj.2378
- 866 Zappa, G., Hoskins, B. J., & Shepherd, T. G. (2015). Improving Climate Change  
867 Detection through Optimal Seasonal Averaging: The Case of the North At-  
868 lantic Jet and European Precipitation. *J. Climate*, 28(16), 6381-6397. doi:  
869 10.1175/JCLI-D-14-00823.1
- 870 Zappa, G., Pithan, F., & Shepherd, T. G. (2018). Multimodel evidence for an atmo-  
871 spheric circulation response to Arctic sea ice loss in the CMIP5 future projections.  
872 *Geophys. Res. Lett.*, 45, 10111019. doi: 10.1002/2017GL076096

873 **List of Tables**

874 • **Table 1.** Correlation coefficients for linear correlation between ocean basin mean  
 875 jet latitude and upper-tropospheric temperature gradient (a). Panel b shows the  
 876 same for the jet strength. Correlation coefficients which are significant at a 95 %  
 877 level are shown in bold letters for better visualization of large linear correlations.  
 878 Positive correlations indicate that increased (decreased) temperature gradients cor-  
 879 respond to (a) a more poleward (equatorward) located and (b) a stronger (weaker)  
 880 jet stream.

881 **List of Figures**

882 • **Figure 1.** Annual-mean SST pattern of the CTL simulation (left) and anomalous  
 883 SST pattern used for the PAT simulation (right). Regions covered by land or more  
 884 than 15 % of sea ice are masked.

885 • **Figure 2.** Response of the annual-mean zonal-mean atmospheric temperature (top),  
 886 zonal wind (middle), and mass stream function (bottom) to a uniform SST increase  
 887 with free clouds (left) (UNI-CTL). The right column shows the difference between  
 888 the response in the locked and free simulations. The green line in each panel shows  
 889 the tropopause height in the control simulation CTL.

890 • **Figure 3.** Mean (crosses) and 95 % significance level (vertical lines) for the dif-  
 891 ference in the jet latitude (left) and jet strength (right) responses between sim-  
 892 ulations with free clouds and simulations with locked clouds. Results are shown  
 893 for each season, ocean basin and global warming setup. Black symbols indicate  
 894 that the responses in simulations with locked and free clouds are statistically sim-  
 895 ilar, grey symbols indicate that they are not statistically similar on a 95 % level.  
 896 Note the different ranges for the vertical axes of the panels.

897 • **Figure 4.** Annual-mean response of the 850 hPa zonal wind,  $u_{850}$ , (left) and storm  
 898 track (right) in the UNI simulations. The total response (top) is decomposed into  
 899 the SST impact (middle) and the cloud-radiative impact (bottom). The black line  
 900 in the left column indicates the jet latitude in the control simulation, the grey con-  
 901 tours in the right column show the storm track in the control simulation (contour  
 902 interval of  $100 \text{ m}^2 \text{ s}^{-2}$ ). For the storm track, the Tropics are not shown. The dots  
 903 indicate where the response is significant at 95 % level.

904 • **Figure 5.** Same as Fig. 4, but for the PAT simulations.

- 905 • **Figure 6.** The left panels show the annual-mean response of ocean basin zonal-  
 906 mean  $u_{850}$  in UNI (straight lines) and PAT (dashed lines). The grey bars indicate  
 907 the jet latitude in CTL derived from the maximum in  $u_{850}$  (small inserted figures).  
 908 The right panels show the poleward jet shift  $\Delta\varphi_{jet}$  versus jet strengthening  $\Delta u_{jet}$ .  
 909 Results are shown for the North Atlantic (top), North Pacific (middle) and South-  
 910 ern Hemisphere (bottom). The total locked response (black) is decomposed into  
 911 cloud-radiative impact (orange) and SST impact (blue).
- 912 • **Figure 7.** Annual-mean zonal-mean response of cloud cover in the simulations with  
 913 free clouds (a, d) and annual-mean zonal-mean change in cloud-radiative heating  
 914 (b, e). The bottom panels depict the vertical-mean changes in cloud-radiative heat-  
 915 ing for a 300 hPa thick layer below the tropopause. Results are shown for the UNI  
 916 (left) and PAT (right) simulations. The black lines in the zonal-mean responses  
 917 indicate the tropopause height in the control simulation, the black line in the maps  
 918 shows the jet latitude in the control simulation.
- 919 • **Figure 8.** Seasonal-mean response of the ocean basin zonal-mean  $u_{850}$  response  
 920 to a uniform (straight line) and patterned (dashed line) SST increase (left) in the  
 921 North Atlantic. The grey bar indicates the jet latitude in the control simulation  
 922 derived from the maximum in  $u_{850}$  (small inserted figures). The right panel shows  
 923 the poleward jet shift  $\Delta\varphi_{jet}$  versus the jet strengthening  $\Delta u_{jet}$ . The total locked  
 924 response (black) is decomposed into cloud-radiative impact (orange) and SST im-  
 925 pact (blue).
- 926 • **Figure 9.** Same as Fig. 8, but for the North Pacific.
- 927 • **Figure 10.** Same as Fig. 8, but for the Southern Hemisphere.
- 928 • **Figure 11.** Correlation between temperature gradient response at 250 hPa,  $\Delta T_{250}$ ,  
 929 and jet strength response,  $\Delta u_{jet}$ , (top) and jet latitude response,  $\Delta\varphi_{jet}$ , (bottom)  
 930 for the North Atlantic, North Pacific and Southern Hemisphere. Filled markers  
 931 are for the response in UNI, open markers for the response in PAT. The total re-  
 932 sponse (black markers) is decomposed into the cloud-radiative impact (orange mark-  
 933 ers) and the SST impact (blue markers). Correlation coefficients  $r$  are marked with  
 934 a star if they are significant on a 95 % level.